

Review

Open Access



Recent progress on alloy-based anode materials for potassium-ion batteries

Qiuran Yang, Qining Fan, Jian Peng, Shulei Chou, Huakun Liu, Jiazhao Wang

Institute for Superconducting and Electronic Materials, Australian Institute for Innovative Materials, University of Wollongong, North Wollongong, New South Wales 2522, Australia.

Correspondence to: Prof. Jiazhao Wang, Institute for Superconducting and Electronic Materials, Australian Institute for Innovative Materials, University of Wollongong, North Wollongong, New South Wales 2522, Australia. E-mail: jiazhao@uow.edu.au

How to cite this article: Yang Q, Fan Q, Peng J, Chou S, Liu H, Wang J. Recent progress on alloy-based anode materials for potassium-ion batteries. *Microstructures* 2023;3:2023013. <https://dx.doi.org/10.20517/microstructures.2022.30>

Received: 26 Sep 2022 **First Decision:** 31 Oct 2022 **Revised:** 12 Dec 2022 **Accepted:** 5 Jan 2023 **Published:** 22 Feb 2023

Academic Editor: Xiaozhou Liao **Copy Editor:** Fangling Lan **Production Editor:** Fangling Lan

Abstract

Potassium-ion batteries (PIBs) are considered as promising alternatives to lithium-ion batteries due to the abundant potassium resources in the Earth's crust. Establishing high-performance anode materials for PIBs is essential to the development of PIBs. Recently, significant research effort has been devoted to developing novel anode materials for PIBs. Alloy-based anode materials that undergo alloying reactions and feature combined conversion and alloying reactions are attractive candidates due to their high theoretical capacities. In this review, the current understanding of the mechanisms of alloy-based anode materials for PIBs is presented. The modification strategies and recent research progress of alloy-based anodes and their composites for potassium storage are summarized and discussed. The corresponding challenges and future perspectives of these materials are also proposed.

Keywords: Potassium-ion batteries, mechanism, alloy-based anode materials

INTRODUCTION

With the rapidly growing demand for energy globally, unrenewable traditional fossil fuels, such as coal, oil and gas, are facing depletion^[1-9]. Clean and renewable energy resources, such as solar, wind and tidal energy, are among the most abundant and promising available resources to take the place of fossil fuels in the



© The Author(s) 2023. **Open Access** This article is licensed under a Creative Commons Attribution 4.0 International License (<https://creativecommons.org/licenses/by/4.0/>), which permits unrestricted use, sharing, adaptation, distribution and reproduction in any medium or format, for any purpose, even commercially, as long as you give appropriate credit to the original author(s) and the source, provide a link to the Creative Commons license, and indicate if changes were made.



future. It is necessary to combine electrical energy storage devices with these renewable energies. Rechargeable lithium-ion batteries (LIBs) are high-energy electrical energy storage devices that have been commercialized for around three decades. LIBs cannot only be used with natural clean renewable energies but are also ubiquitous in our daily lives for powering electronics, including cell phones, electric cars and laptops. However, their high-cost resources and the uneven distribution of lithium in the Earth's crust make it imperative to develop alternatives to LIBs with comparable performance^[10-12].

Potassium-ion batteries (PIBs) are possible alternatives to LIBs. Compared to lithium resources in the Earth's crust, potassium resources are significantly more abundant in the Earth's crust at ~1.5 wt.%. The price of potassium salts, such as K_2CO_3 , is far less compared to Li_2CO_3 . In addition to the lower cost of potassium resources, inexpensive aluminum current collectors can be used together with PIBs to offer a low-cost method based on economical salts^[13-15]. In addition, potassium ions exhibit much weaker Lewis acidity, which results in smaller solvated ions compared to lithium and sodium ions. Therefore, the ionic conductivity of solvated K^+ is higher than that of lithium and sodium ions^[16,17]. In addition, the lower energy required to dissolve potassium ions also results in their fast diffusion kinetics.

Similar to LIBs and sodium-ion batteries (SIBs), the study of cathode materials for PIBs mainly includes layered transition metal oxides, Prussian blue analogs (PBAs) and polyanionic compounds. Layered transition metal oxides based on K_xMO_2 ($x \leq 1$, $M = Co, Cr, Mn, Fe$ or Ni) deliver high capacity but face the critical problems of multiple plateaus and large structural changes during potassium-ion intercalation/deintercalation^[18,19]. The chemical formula of PBAs is represented as $K_xM1[M2(CN)_6]_nH_2O$ ($0 \leq x \leq 2$), where $M1$ and $M2$ represent various metals, such as Fe, Cr, Co and Ni ^[20-23]. One advantage of PBAs is their three-dimensional (3D) open frameworks that are available for large K^+ to diffuse. Another advantage of PBAs in PIBs is their high average working potential of 3.5 V. Currently, the disadvantages of PBAs are their low conductivity and bulk density^[24,25]. Polyanionic compounds also have 3D open channels that are available for the fast diffusion of large K ions^[26,27]. The study of PIB cathode materials makes the development of full-cell PIBs possible and promising.

The search for anode materials is also an important part of PIB research and development. Commercialized graphite has been widely applied in LIBs; however, it is not an ideal anode candidate. Even though graphite has a theoretical capacity of ~280 $mAh\ g^{-1}$ from the formation of KC_8 ^[28,29], the large radius of the potassium ions results in sluggish diffusion kinetics and the formation of an unstable SEI. Therefore, graphite anodes deliver limited experimental capacity and cycling life in PIBs. As a result, it is crucial to develop high-performance anode materials with high specific capacity and long cycling life for practical application. In the past five years, there has been a large volume of research regarding electrode materials for PIBs, including metal-organic structure design^[30,31] for electrodes and the modification of electrode surfaces^[32,33]. However, there have been few review papers that focus on anode materials for PIBs, especially on high-performance alloy-based anode materials, including their modification and mechanisms in PIBs^[34]. In this review, we comprehensively summarize the current understanding of alloy-based anode materials and their composites for PIBs, as shown in [Figure 1](#), including their mechanisms, modification strategies and recent research progress for potassium storage. The challenges and future perspectives corresponding to these materials are also presented.

Alloy-based elements can deliver high-capacity anode materials via the formation of potassium-rich materials. For example, Bi has a high theoretical capacity of 385 $mAh\ g^{-1}$ PIBs. Sb has a high theoretical capacity of 687 $mAh\ g^{-1}$. P has the highest theoretical capacity among alloy-based anodes in PIBs of 865 $mAh\ g^{-1}$. Ge has a high theoretical capacity of 369 $mAh\ g^{-1}$ and Sn has a theoretical capacity of

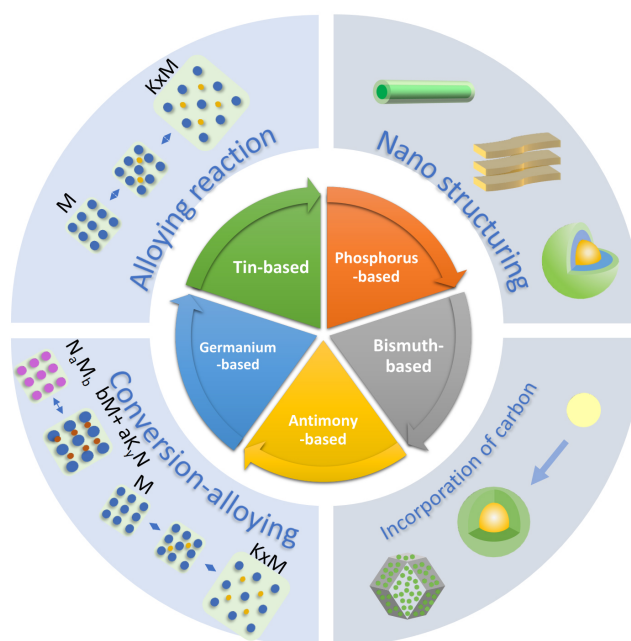


Figure 1. Alloy-based anode materials for PIBs.

226 mAh g⁻¹ in PIBs. We calculated the theoretical volumetric and gravimetric capacities of P, Bi, Sb, Ge and Sn, as shown in Figure 2. The volumetric capacities are calculated based on the density of the materials and their theoretical weight capacities. Based on the calculation, the volumetric capacities of P, Bi, Sb, Ge and Sn are 1574, 2753, 4597, 1964 and 1652 mAh cm⁻³. While the study of alloy-based anode materials in LIBs and SIBs has been extensive in recent years, the study of PIBs remains at the early stage. Therefore, high-capacity alloy-based anodes are worthy of further study.

Potassium storage mechanism of alloy-based anode materials for PIBs

Potassium storage in anode materials for PIBs can be classified into three categories: intercalation, alloying and conversion. The intercalation reaction results in a smaller volume change and higher reversible capacity than the other potassium storage mechanisms. During the intercalation reaction, potassium ions are inserted into the anode material and form a new phase. This reaction usually takes place in materials with a layered structure, such as graphite^[35,36] and K₂Ti₄O₉. The alloy-based anode material SnS₂ undergoes an intercalation reaction in the first step and conversion and alloying reactions in the following steps. The intercalation reaction can be expressed as $M_xN_y + aK^+ + ae^- \leftrightarrow K_aM_xN_y$. Typical intercalation reactions deliver high reversible capacity because of the low volume change of the crystal during the electrochemical reaction. Due to the large radius of the potassium ion, however, anode materials with an intercalation-type potassium storage process experience a larger volume change and have less reversible capacity in their performance in LIBs and SIBs.

Compared to the intercalation reaction, alloying-reaction materials undergo a larger volume change and have higher theoretical capacities. Alloying-type materials react with K to form the binary compound K_xM. The reaction process can be expressed as $aM + bK^+ + be^- \leftrightarrow K_bM_a$. In this reaction, M represents Sn, Bi, Sb, P or Ge. These alloying-type materials can form binary metallic materials that undergo conversion-alloying reactions, in which the compound decomposes and further alloys with potassium. For example, Sn₄P₃ undergoes the following reaction: $Sn_4P_3 + 11K \leftrightarrow 4KSn + 3K_3P$ ^[26]. Similarly, Sb₂Se₃ goes through the following conversion-alloying reaction: $Sb_2Se_3 + 12K^+ + 12e^- \leftrightarrow 3K_3Sb + 2K_2Se_3$ ^[27].

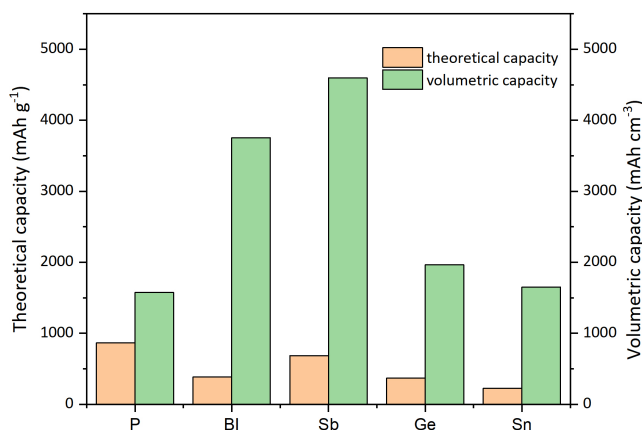


Figure 2. Theoretical and volumetric capacities of P, Bi, Sb, Ge and Sn.

These conversion-alloying type reactions can be expressed as $M_xN_y + (xn + ym)K^+ + (xn + ym)e^- \leftrightarrow xK_nM + yK_mN$. Similarly, the metallic compounds that go through conversion-alloying type reactions also deliver high theoretical capacities. For example, Sn_4P_3 delivers a high capacity of 585 mAh g^{-1} while the experimental capacity is $\sim 384 \text{ mAh g}^{-1}$.

Challenges

Although alloying-type anode materials deliver high theoretical capacities, their practical reversible capacities are far below their theoretical capacities. The severe volume change causes capacity decay, poor cycle life, inferior rate performance, sluggish kinetics and limited cycling lifespans.

The initial capacity is a key factor, especially for the anode material, which contributes to the energy density of the full cell. The significant volume changes during the discharge-charge processes cause pulverization of the active materials, which results in discontinuous particles. Due to the large resistance within the particles, the potassium ions cannot be fully extracted, which results in irreversible capacity and low Coulombic efficiency. In addition, the stress generated in the electrode during the discharge process damages the SEI, resulting in its breakdown and the reformation of a new SEI film. In addition, the pulverized particles inevitably go through crystallization and aggregation, which increase the diffusion length of the potassium ions and also lead to irreversible capacity loss. The decreasing reversible capacity results in a rapid capacity drop and short cycling life.

ALLOY-BASED ANODES FOR PIBS

Phosphorus-based anode materials

Among alloying-typed anode materials, phosphorus is very attractive because it has a high theoretical capacity of 2596 mAh g^{-1} in LIBs and SIBs and a low work potential ($\sim 0.3 \text{ V vs Na/Na}^+$). In PIBs, it has a high theoretical capacity of 2590 mAh g^{-1} based on the three-electron alloying mechanism.

Mechanism of phosphorus and metal phosphides in PIBs

There are three main types of phosphorus in nature, namely, white phosphorus (WP), red phosphorus (RP) and black phosphorus (BP). WP is toxic and has a low ignition point, so it is unsuitable as an electrode. RP exists in a non-crystalline form and has a low conductivity of $10^{-12} \text{ S m}^{-1}$. BP is a layered structure semiconductor material, which has a wide interlayer spacing of 5.2 \AA and a higher conductivity at 300 S m^{-1} . BP has a high theoretical capacity of 2600 mAh g^{-1} for LIBs and NIBs and also has a low diffusion barrier of 0.035 eV for Li^+ and 0.064 eV for Na^+ , which makes it a promising anode material to explore for PIBs. There

are two interlayer migration paths: zigzag- and armchair-type migration paths. The zigzag path has a much lower energy barrier. Based on calculations, K has the lowest energy barriers for both paths compared to Li and Na, which endow PIBs with fast discharging and charging. The corresponding voltage can be calculated based on the following equation:

$$V = -\frac{\mu}{q} = -\frac{\Delta G}{e\Delta N} \quad (1)$$

where V , μ , q , G , e and N are the voltage, chemical potential, charge, absolute electron charge, Gibbs free energy and the number of K ions, respectively.

Thus, the calculated potassium-ion insertion process is $\text{BP} \rightarrow \text{K}_2\text{P}_3 \rightarrow \text{KP}$. A previous study of the potassiation mechanism indicated that the final product was $\text{KP}^{[36-39]}$, which was first revealed by the group of Glushenkov. Compared to this result, a further study by Jin *et al.* used X-ray absorption near-edge structure and *ex-situ* X-ray diffraction (XRD) methods to analyze the mechanism^[38]. The results demonstrated that the potassiation process of BP was $\text{K}^+ + \text{P} + \text{e}^- \rightarrow \text{KP}$. An RP-based nanocomposite was studied by the group of Xu^[39]. The composite was synthesized by anchoring RP nanoparticles on a 3D nanosheet framework. The reaction mechanism of the composite was explored by transmission electron microscopy (TEM) and selected area electron diffraction (SAED). Based on the first cycle reaction results, KP was proposed to be the final product, corresponding to a capacity of 865 mAh g^{-1} , which is lower than the theoretical capacity. Yu *et al.* synthesized an RP/carbon nanocomposite by embedding RP into free-standing nitrogen-doped porous hollow carbon^[40]. Using *in-situ* Raman spectroscopy and *ex-situ* XRD, the final product in the discharge process was directly proved to be K_4P_3 .

One challenge for BP and RP in the potassiation process compared to lithiation is the lower capacity. A BP-graphite composite had only 42% of the capacity for lithiation. The other issue is their large volume expansion. BP-graphite showed a 200% volume expansion when discharged to $0.01 \text{ V}^{[41]}$.

The large volume expansion during the potassiation process and low conductivity of RP severely limit the application of phosphorus-based anode materials in PIBs. To overcome this, active (Sn, Ge and Se) and inactive metals (Co, Fe and Cu) have been hybridized with P to form phosphides. During the discharge process, the decomposed nanocrystals form a conductive and elastic matrix to enable faster charge transfer and hinder volume expansion. In addition, the active metals become alloyed with potassium ions and also make contributions to the capacity. Metal phosphides can be classified into two categories based on active and inactive metals. For the inactive metals, the storage mechanism reaction can be summarized as follows:



For the active metal phosphides, the reaction can be summarized as follows:



The original phosphide M_xP_y decomposes and the phosphorus is converted into $K_{3-x}P$, while inactive metal M is dispersed as a matrix and active metal M is also alloyed with K to produce K_nM .

Unlike phosphides in LIBs and SIBs, to date, the reported phosphide potassiation mechanisms are conversion-type mechanisms. For example, the electrochemical reaction of Sn_4P_3 in PIBs is a typical conversion reaction, as first studied by the group of Guo based on an *in-operando* synchrotron XRD investigation. In the initial discharge stage, Sn_4P_3 breaks into Sn particles and the P component precipitates in an amorphous form to react with potassium. Sn is alloyed with K and the KSn phase is formed. K_3P_{11} further reacts with K, starting from ~ 0.17 V. The reaction process could be divided into three steps, namely, $\text{Sn}_4\text{P}_3 + (9-3x)\text{K} \leftrightarrow 4\text{Sn} + 3\text{K}_{3-x}\text{P}$, $23\text{Sn} + 4\text{K} \leftrightarrow \text{K}_4\text{Sn}_{23}$ and $\text{K}_4\text{Sn}_{23} + 19\text{K} \leftrightarrow 23\text{KSn}$, as shown in Figure 3A^[42]. The Sn_4P_3 @carbon fiber electrode delivered cycling stability and a high-rate capability of 160.7 mAh g^{-1} after 1000 cycles at a current density of 500 mA g^{-1} . Like Sn_4P_3 , GeP_5 also has a similar conversion reaction. Based on *in-operando* synchrotron XRD measurements, a two-step reaction was observed as follows: $\text{GeP}_5 + 20/3\text{K} \leftrightarrow 5/3\text{K}_4\text{P}_3 + \text{Ge}$, $\text{Ge} + \text{K} \leftrightarrow \text{KGe}$. These two steps can be summarized into one equation as follows: $3\text{GeP}_5 + 23\text{K} \leftrightarrow 5\text{K}_4\text{P}_3 + 3\text{KGe}$ ^[43]. This potassiation process is shown in Figure 3B. Similarly, in the first stage of the reaction, GeP_5 decomposes into Ge and P particles and the P component reacts with K to form K_4P_3 . In the following stage of the reaction, Ge alloys with K to form KGe. Se is also an active element that can form K_2Se through a two-electron transfer reaction. Se_3P_4 exhibited a high reversible capacity of 1036 mAh g^{-1} in PIBs^[44]. Based on *ex-situ* XRD and X-ray photoelectron spectroscopy (XPS) results, Se_3P_4 delivered a reversible conversion-type reaction as follows: $\text{Se}_3\text{P}_4 + (18-4x)\text{K}^+ + 18\text{e}^- \leftrightarrow 4\text{K}_{3-x}\text{P} + 3\text{K}_2\text{Se}$ ^[44], as shown in Figure 3C and D. The inactive material, such as Cu_3P , undergoes the reaction of $2\text{Cu}_3\text{P} + (3-x)\text{K}^+ + (3-x)\text{e}^- \leftrightarrow \text{K}_{3-x}\text{P} + 6\text{Cu} + \text{P}(\text{amorphous})$ and the final discharge product is also K_3P ^[45].

In summary, until now, the reported phosphide potassiation mechanisms have been conversion-type mechanisms, which are different from phosphides in SIBs and LIBs. In the first discharge step, the phosphide decomposes into metal and phosphorus. After the anode has been fully discharged, the active metal reacts with K and forms K_nM compounds, with the phosphorus alloyed with K to form K_mP .

Modification strategies for P and phosphides

Carbon materials, including nanosheets^[39], nanofibers^[40] and graphite^[45], have been applied in phosphorus and phosphides. The hybridization of phosphorus and phosphides with carbon materials has been proven to be an efficient method to improve the electrochemical performance. The introduction of carbon can enhance the electron conductivity, accommodate the volume change and also shorten the potassium-ion diffusion length. Furthermore, the induced carbon can form covalent P-C interfaces to prevent edge reconstruction and ensure ion insertion and diffusion^[35]. In addition, the formation of P-C bonds^[46-49] by hybridizing BP with carbon materials can afford high capacity and cycling stability in PIBs by connecting particles. This can also be seen from the work of Verma *et al.*, where the electrochemical performance of SnP_3 was efficiently improved by hybridizing with carbon^[50]. The electrode maintained a reversible capacity of 225 mAh g^{-1} after 80 cycles, which was an improvement compared to the previous rapid capacity drop of the SnP_3 electrode in cycling performance. Similarly, the group of Zhu^[51] designed a flexible and hierarchically porous 3D graphene/FeP composite via a one-step thermal transformation strategy. The interconnected porous conducting network sufficiently buffered stress due to the nano-hollow spaces and greatly promoted the charge transfer. Thus, the composite delivered a high-capacity retention of 97.2% over 2000 cycles at a high rate of 2 A g^{-1} in PIBs.

Synthesizing nanostructured phosphorus and phosphide materials, such as yolk-shell structures^[52], hollow structures and nanowires, is another efficient method to improve the electrochemical performance of phosphide and phosphorus anodes. For example, Yu *et al.* designed a one-dimensional electrode by embedding RP into free-standing nitrogen-doped porous carbon nanofibers^[40]. This design was favorable for reducing the absolute strain and preventing pulverization and agglomeration. As can be seen from their

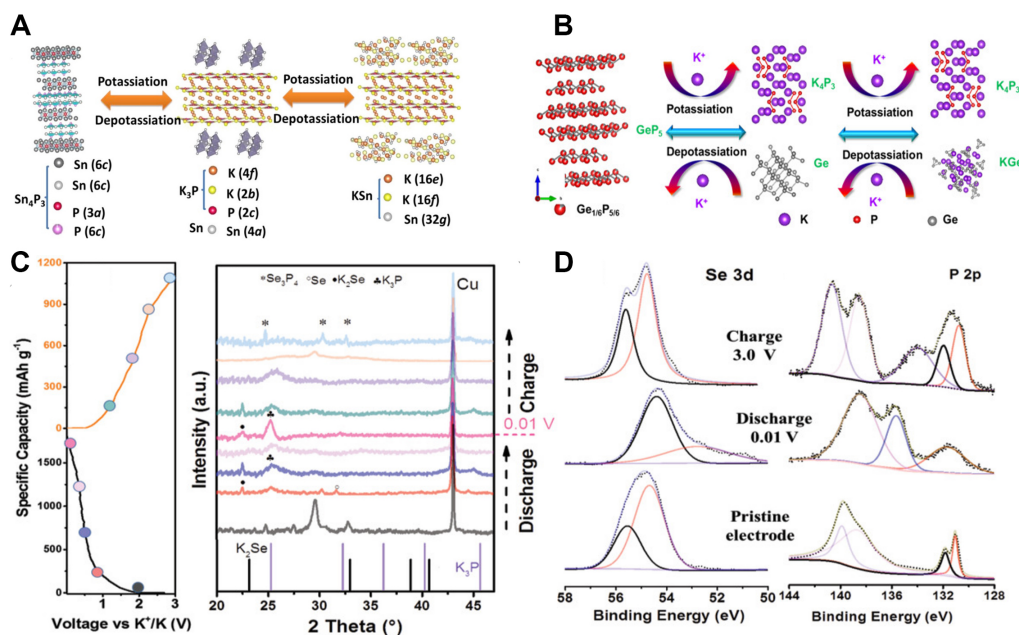


Figure 3. (A) Potassiation/depotassiation process in $\text{Sn}_4\text{P}_3/\text{C}$.^[42] Copyright 2017, American Chemical Society. (B) Potassiation/depotassiation process in GeP_5 electrodes.^[43] Copyright 2018, Elsevier. (C) Discharge/charge curves of $\text{Se}_3\text{P}_4/\text{C}$ and XRD patterns of $\text{Se}_3\text{P}_4/\text{C}$ anode in the first cycle at different cut-off voltages. (D) XPS spectra of $\text{Se}_3\text{P}_4/\text{C}$ electrode at different cut-off voltage states.^[44] Copyright 2020, Wiley VCH.

images, during potassiation, the thickness changed from 74 to 93 nm with a volume expansion of only 26%. Because of its nanowire structure, the composite exhibited a high reversible capacity of 465 mAh g^{-1} after 800 cycles at a high current density of 2 A g^{-1} . The yolk-shell and hollow structures have void space that can accommodate the significant volume change, so that particles can expand without deforming the carbon shell during potassiation^[52]. The potassium-ion transport in BP is mostly in the armchair direction, as shown in Figure 4A and B. The potassiation process includes several steps with the formation of binary phosphide, as displayed in Figure 4C. Figure 4D shows that the composite delivered stable cycling performance with a reversible capacity of 205 mAh g^{-1} after 300 cycles. A comparison of the electrochemical performance of phosphides and their composites is shown in Table 1.

The theoretical capacity of phosphorus in PIBs is 2596 mAh g^{-1} based on the three-electron alloying mechanism; however, the experimental capacity varies with different final products. There are currently three known types of final potassiation products of phosphides, namely, KP , K_4P_3 and K_3P . In addition, the final and intermediate products of phosphides in PIBs are different even though the reactions are typically conversion-alloying mechanisms. Due to the significant volume change during the potassiation processes of phosphorus and phosphides and the low conductivity of phosphorus, various modification methods have been applied. Synthesizing nanostructures, such as yolk-shell, nanowire and hollow structures, and hybridization with graphite, graphene, nanotubes and porous carbon have significantly improved the electrochemical performance.

Bi-based electrodes for PIBs

Bi is an attractive low-cost and non-toxic anode material. Due to its large interlayer spacing (d) along the c -axis, $d(003) = 3.95 \text{ \AA}$, Bi is a promising anode material for PIBs. The theoretical weight capacity of Bi is 385 mAh g^{-1} . Furthermore, Bi has a high theoretical volumetric capacity of 3800 mAh cm^{-3} , which also makes it a novel potential anode.

Table 1. Summary of electrochemical performance of P-based anodes for PIBs

	Anode materials	Synthesis method	Modification methods	Redox potential (vs. K/K')	Current density (mA g ⁻¹)	Initial capacity (potassiation) (mAh g ⁻¹)	Initial depotassiation	1st CE	Reversible capacity	Best rate capability	Electrolyte	Ref.
BP	BP/graphite	Vaporization-condensation	Hybridized with graphite	-0.5 V	250	1430	600	42%	340 mAh g ⁻¹ after 100 cycles at current density of 0.75 A g ⁻¹	340 mAh g ⁻¹ at 750 mA g ⁻¹	1 M KPF ₆ in EC:DEC	[38]
RP	RP/carbon nanosheet	Heat treatment	Hybridized with carbon nanosheets/design of 2D nanostructure	0.16-1.0 V	100	1212	715	59%	427.4 mAh g ⁻¹ after 40 cycles at current density of 100 mA g ⁻¹	323.7 mAh g ⁻¹ at 2000 mA g ⁻¹	0.8 M KPF ₆ in EC:DEC	[39]
	Yolk-shell FeP/C		Hybridized with carbon/design of 3D nanostructure	0.05-1.2 V	100	561	264	47%	205 mAh g ⁻¹ after 300 cycles	37 mAh g ⁻¹ at 2000 mA g ⁻¹	0.8 M KPF ₆ in EC:DEC	[52]
Phosphide (inactive metal)	CuP ₂ /Carbon nanosphere	Wet chemical and heat treatment	Hybridized with carbon/design of 2D nanostructure		100	-700	-490	~70%	400 mAh g ⁻¹ over 300 cycles	170 mAh g ⁻¹ at 2 A g ⁻¹	4 M KFSI in DME	[53]
	CoP/C	Heat treatment	Hybridized with carbon	0.01-1.26 V	50	706	301	42.7%	40 mAh g ⁻¹ at 1000 mA g ⁻¹ after 400 cycles	106 mAh g ⁻¹ at 1000 mA g ⁻¹	1 M KPF ₆ EC:PC	[54]
Phosphide (active metal)	SnP ₃ /C	Mechanical milling	Hybridized with carbon	0.01-0.8 V	50	697	410	58.8%	408 mAh g ⁻¹ after 50 cycles	225 mAh g ⁻¹ at 500 mA g ⁻¹	0.75 M KPF ₆ EC:DEC	[50]
	Se ₃ P ₄ /C	Mechanical milling and heat treatment	Hybridized with carbon	1.3-1.9 V 0.37 V	50	1505	1036	68.9%	783.4 mAh g ⁻¹ after 100 cycles at 100 mA g ⁻¹	388 mAh g ⁻¹ at 1000 mA g ⁻¹	0.8 M KPF ₆ EC:DEC:FEC	[44]
	Sn ₄ P ₃ /C	Mechanical milling	Hybridized with carbon	0.01-1.15 V	50	588.7	384.8	65%	307.2 mAh g ⁻¹ at 50 mA g ⁻¹ after 50 cycles	221.9 mAh g ⁻¹ at 1000 mA g ⁻¹	1 M KPF ₆ EC:DEC	[51]
	Sn ₄ P ₃ /carbon fiber	Mechanical milling and electrospinning	Hybridized with carbon/design of nanostructure	0.01-0.5 V	50	803	514	64%	403 mA g ⁻¹ at 50 mA g ⁻¹ after 200 cycles	160.7 mA g ⁻¹ after 1000 cycles at 500 mA g ⁻¹	1 M KFSI EC:DEC	[55]
	Sn ₄ P ₃ /C	Wet chemical and heat treatment	Hybridized with porous carbon/design of nanostructure	0.01-0.4 V 1.1-1.6 V	100	845	431	51%	315 mA g ⁻¹ at 1000 mA g ⁻¹ after 100 cycles	186 mAh g ⁻¹ at 2000 mA g ⁻¹	0.8 M KPF ₆ EC:DEC	[56]
	GeP ₅	Mechanical milling	Nanostructural design	0.10-0.45 V	50	2038	934	45.81%	495.1 mA g ⁻¹ at 50 mA g ⁻¹ after 50 cycles	213 mA g ⁻¹ at 500 mA g ⁻¹ after 2000 cycles	1 M KFSI EC:DEC	[43]

CE: Coulombic efficiency.

K-ion storage mechanism of Bi-based anodes

Based on the K-Bi equilibrium diagram with the KBi_2 , K_3Bi_2 , $\text{K}_3\text{Bi}(\alpha)$, $\text{K}_3\text{Bi}(\beta)$ and K_5Bi_4 phases, Huang *et al.* first studied the potassium-ion storage mechanism in Bi microparticles^[57]. They revealed stepwise $\text{Bi} \rightarrow \text{KBi}_2 \rightarrow \text{K}_3\text{Bi}_2 \rightarrow \text{K}_3\text{Bi}$ dealloying-alloying electrochemical processes after the initial surface potassiation. Similarly, a bulk Bi anode delivered a reversible three-step reaction during cycling, with K_3Bi as the fully discharged product^[58]. Bi microparticles have the same mechanism as shown in Figure 5A and B, with K_3Bi as the final discharged product. As shown in Figure 5C, the observation of K_5Bi_4 during the potassiation process was first reported by the group of Guo^[59]. They found a different transition process, in which the potassiation of Bi nanoparticles proceeds through a solid-solution reaction, followed by a two-step reaction, corresponding to $\text{Bi} \rightarrow \text{Bi}(\text{K})$ and $\text{Bi}(\text{K}) \rightarrow \text{K}_5\text{Bi}_4 \rightarrow \text{K}_3\text{Bi}$. Xie *et al.* constructed dual-shell-structured Bi box particles and microsized Bi, which had different appearances during the transformation from K_3Bi_2 to K_3Bi under a low current density^[60]. In the case of nanostructured Bi, the K_3Bi_2 phase went through a transformation to K_3Bi , as shown in Figure 5D. In comparison, the microstructure of Bi retained the K_3Bi_2 phase and no significant K_3Bi phase was formed. Interestingly, when the current was increased, no significant K_3Bi_2 or K_3Bi phase was observed, indicating that the main mechanism was a surface-driven adsorption reaction under a high current.

The study of the potassiation mechanism in Bi-based alloys has also attracted significant attention. The reaction process includes two stages. The first step was an intercalation reaction: $\text{Bi}_2\text{S}_3 + x\text{K}^+ + xe^- \rightarrow \text{K}_x\text{Bi}_2\text{S}_3$. The second step was a conversing-alloying reaction: $\text{K}_x\text{Bi}_2\text{S}_3 + (6-x)\text{K}^+ + (6-x)xe^- \rightarrow 3\text{K}_2\text{S} + 2\text{Bi}$ and $\text{Bi} + 3\text{K}^+ + 3e^- \rightarrow \text{K}_3\text{Bi}$ ^[61]. Chen *et al.* also studied the reaction mechanism of Bi_2Se_3 using *in-situ* operando XRD^[62]. The results indicated that the potassiation process also undergoes an intercalation reaction in the first steps, with a conversion-alloying reaction in the following step. The electrochemical process was summarized as follows: $2\text{Bi}_2\text{Se}_3 + 4x\text{K}^+ + 4xe^- \rightarrow 4\text{K}_x\text{Bi}_2\text{Se}_3$, $\text{K}_x\text{Bi}_2\text{Se}_3 + (6-x)\text{K}^+ + (6-x)e^- \rightarrow 3\text{K}_2\text{Se} + \text{Bi}$ and $\text{Bi} + 3\text{K}^+ + 3e^- \rightarrow \text{K}_3\text{Bi}$ ^[62].

The above results illustrate the diverse potassiation mechanisms. The differences in the potassiation and depotassiation processes were mainly because of the following reasons: (1) the mechanisms are strongly dependent on the sizes of the materials; (2) the unique structure of the Bi-based anodes; and (3) the current density of the electrochemical reaction. The small particle sizes, well-constructed nanostructure and low current density resulted in full potassiation and transformation that involved several transition phases.

Modification strategies for Bi-based anodes

The main challenge for Bi-based anode materials is the pulverization and fracturing of the electrode during the cycling process that are driven by the significant volume changes, resulting in capacity fading.

To improve the electrochemical performance of Bi, various methods have been applied. One method is to combine Bi with carbon materials. Various porous carbon materials have been applied, such as porous graphene^[63] and carbon nanosheets^[64]. Both of these porous carbons were synthesized using freeze drying assisted by a pyrolysis method. The Bi/macroporous graphene composite delivered an excellent rate performance of 185 mAh g^{-1} at a high current density of 10 A g^{-1} . This was because the 3D interconnected macroporous graphene framework could provide robustness to maintain the structural stability.

N-doped carbons were demonstrated to simultaneously improve the conductivity and electrochemical activity of carbon materials and were applied in combination with Bi^[63,64], as shown in Figure 6A-F. Similarly, Shi *et al.* designed a multicore-shell Bi-N nanocomposite using a facile self-template method. The anode delivered a stable performance of 266 mAh g^{-1} after 1000 cycles at 20 A g^{-1} , as shown in Figure 6G-I^[65]. Li *et al.* used hollow N-doped carbon to coat bismuth nanorods, which showed the best long-cycling

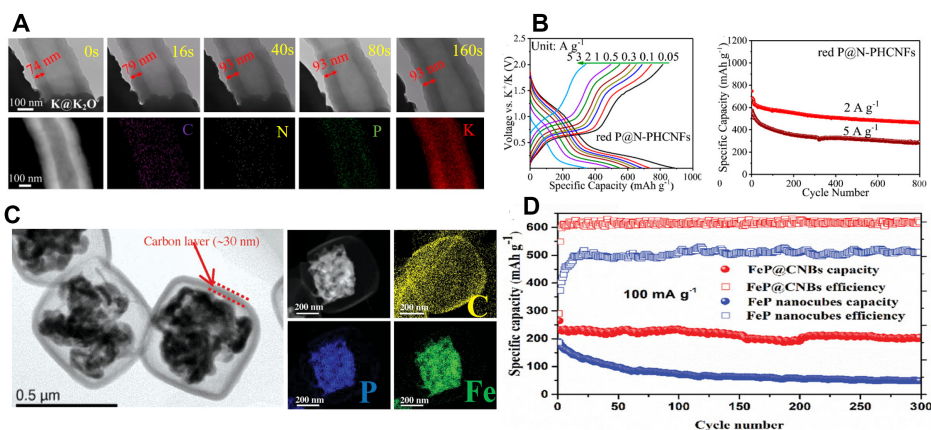


Figure 4. (A) Time-lapse TEM images for single RP@N-PHCNFs, where PHCNFs are porous hollow nanofibers, during potassiation process. (B) Charge/discharge profiles of RP@N-PHCNF electrode at various current densities and cycling performance of RP@N-PHCNF anodes^[40]. Copyright 2019, American Chemical Society. (C) Bright-field TEM images and elemental mapping analysis of FeP@CNBs, where CNBs are carbon nanoboxes. (D) Cycling performance of FeP@CNBs and FeP nanocubes at 0.1 A g⁻¹^[52]. Copyright 2019, Wiley VCH.

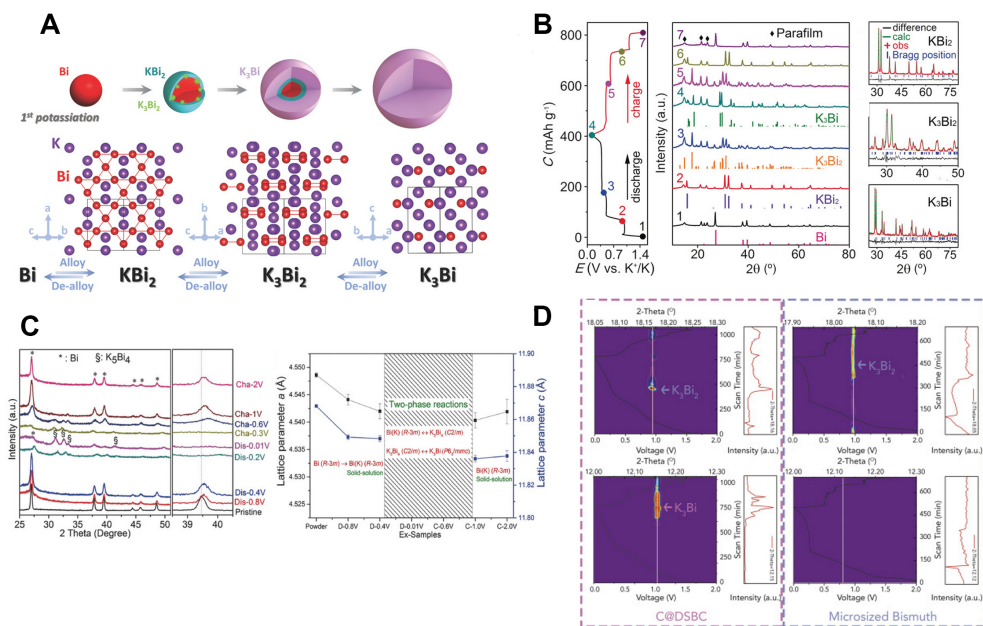


Figure 5. Different potassiation and depotassiation mechanisms of Bi. (A) Alloying and dealloying processes in microparticle Bi electrode^[57]. Copyright 2018, Wiley-VCH. (B) Discharge/charge curves for XRD patterns and XRD patterns with Rietveld refinement of intermediates of porous Bi electrode^[58]. Copyright 2018, Wiley-VCH. (C) *Ex-situ* XRD patterns collected at different charge/discharge states with refined lattice parameters and proposed potassiation/depotassiation mechanism of Bi@reduced graphene oxide (rGO) electrode^[59]. Copyright 2018, Wiley-VCH. (D) *Operando* XRD pattern with superimposed voltage profiles of C@DSBC and microsized Bi^[60]. Copyright 2019, Elsevier.

performance among the Bi/C composite anodes and had a high capacity of 297 mAh g⁻¹ over 1000 cycles at 20 C^[66].

Another important method to improve the electrochemical performance of Bi is nanoengineering. In addition to the multicore-shell structures mentioned above, which are typical designs for Bi-based anodes, Xie *et al.* designed a dual-shell bismuth box (DSBC) anode^[60], which delivered a high-rate capacity of

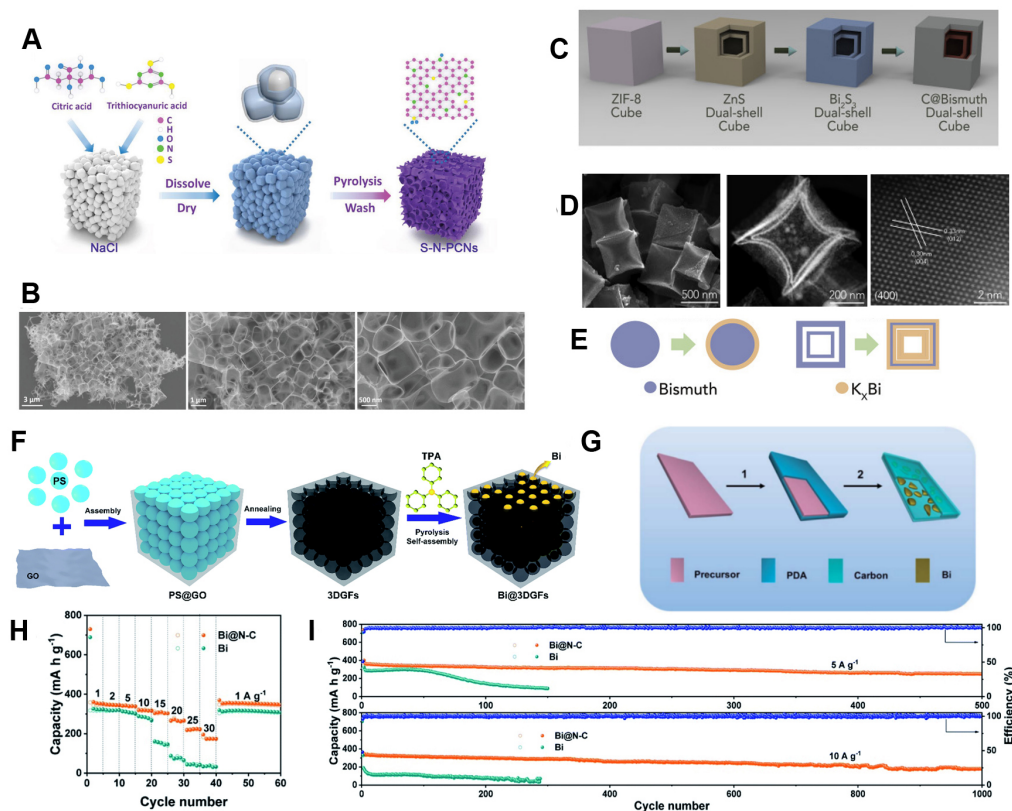


Figure 6. (A) Schematic illustration and (B) TEM images of Bi@porous carbon composite^[64]. Copyright 2019, Wiley-VCH. (C) Schematic illustration of synthetic procedure and (D) TEM images of C@DSBC. (E) Schematic illustration of superior electrochemical performance of C@DSBC under high current density^[60]. Copyright 2019, Elsevier. (F) Schematic illustration of synthesis procedure for Bi@3D graphene foams (GFs)^[63]. Copyright 2019, Royal Society of Chemistry. (G) Schematic illustration of synthesis of Bi@N-C composite. (H) Rate performance of Bi@N-C and Bi anodes from 1 to 30 A g⁻¹ and (I) long-term cycling stability of Bi@N-C and Bi anodes at high rates of 5 and 10 A g⁻¹^[65]. Copyright 2020, Royal Society of Chemistry.

222 mAh g⁻¹ at a current density of 0.8 A g⁻¹. The as-prepared anode had a potassium storage potential of ~0.7 V. The anode material had a large surface area, which could offer more sites for electrochemical reactions, resulting in a lower average oxidation stage and indicating a higher energy density. Designing two-dimensional (2D)-layered structures is another efficient nanoengineering method. The layered structure and weak van der Waals forces of Bi offer the possibility of exfoliating Bi into 2D-layered structures. Recently, bismuthene was prepared using an ultrasonication-assisted electrochemical exfoliation method^[67-69]. The as-prepared anode delivered highly stable capacities of 423, 356, 275 and 227 mAh g⁻¹ at current densities of 2.5, 5, 10 and 15 A g⁻¹, respectively. It delivered a stable cycling performance with a capacity of over 200 mA h g⁻¹ at 20 A g⁻¹ after 2500 cycles.

As reported, K⁺ ions have lower Lewis acidity than Li⁺ and Na⁺ ions, indicating a lower ability to accept electrons from anions and solvents. Thus, potassium salts have a lower degree of dissociation. The salt solubility is based on the Born-Haber cycle:

$$\Delta G_{dissolution}^0 = \Delta G_{solvation}^0 - \Delta G_{lattice}^0 \quad (4)$$

where $\Delta G_{dissolution}^0$ represents the Gibbs free energy of dissolution and $\Delta G_{lattice}^0$ and $\Delta G_{solvation}^0$ represent the Gibbs energies of the salt lattice and the solvation of salts, respectively^[70].

To date, the reported potassium salts used in Bi-based anodes are KPF₆ and potassium bis(fluorosulfonyl)imide (KFSI). KPF₆ has a high calculated Kapustinskii lattice energy of 564.9 kJ mol⁻¹, while KFSI has a lower lattice energy^[70], indicating that KFSI has higher solubility compared to KPF₆. KFSI also has higher ionic conductivity than KPF₆ and KFSI-based electrolytes can form more stable SEI layers. This is because the FSI⁻ anion has weak S-F bonds that make it easier to form KF, which is a main component in the SEI layer^[71].

Zhang *et al.* first used KFSI as the electrolyte salt in Bi-based anode materials with ethylene carbonate (EC) and diethyl carbonate (DEC) as solvents^[59]. The results indicated that the KFSI-based electrolyte had better cycling performance compared to the KPF₆-based electrolyte. The morphological and mechanical properties of the KFSI and KPF₆ electrolytes were investigated using atomic force microscopy, Kelvin probe microscopy and TEM. The results demonstrated that the KPF₆-based electrolyte formed a thicker and more heterogeneous SEI layer, while the SEI layer in the KFSI-based electrolyte was more uniform.

Ether solvents are the most used solvents for Bi-based anode materials. As discussed above, the highest occupied molecular orbital (HOMO) and lowest unoccupied molecular orbital (LUMO) energy levels of solvents or anions are lower when solvents or anions modify a cation through coordination. This is because an electron pair is donated to the cation. Thus, an anode with chemical potential $\mu > E_{lumo}$ can spontaneously transfer electrons to the LUMO of the electrolyte and trigger reduction. In ether solvents, the HOMO values of the ion-solvent complexes are of the order of Li⁺ > Na⁺ > K⁺, while the LUMO values follow the order of Na⁺ > K⁺ > Li⁺^[13]. Therefore, the reduction and oxidation products in ether-based PIBs are complicated. Huang *et al.* first used dimethoxyethane (DME) as their ether-based solvent in Bi-based PIBs^[57]. Using XPS and *in-situ* Raman spectroscopy to probe the SEI components, it was revealed that C-C(H), C-O, C=O and K-O bonds were formed and the SEI consisted of organic and inorganic compounds, such as (CH₂CH₂-O)_nK, (CH₂CH₂-OCH₂-O)_nK, (RCO₂K) and K₂O_x. In addition, the oligomers were from the reduction of DME. This ether-derived SEI possessed better mechanical flexibility because of the strong binding in alkoxy (O-K) edge groups and the elastic properties of the as-formed SEI. This SEI could effectively restrain the volume change of the particles. Density functional theory (DFT) calculations were performed to analyze the interaction between Bi and DME. Three adsorption models of a DME molecule on the (012) crystal plane of Bi were applied. Based on the models, the adsorption energies were 1.76, 0.65 and 0.60 eV. These adsorption energies were higher than for ester-based propylene carbonate (PC) molecules on Bi, which favored the formation of a 3D porous structure in potassiation and depotassiation^[58].

Generally, electrolytes for Bi-based PIBs contain 1 M K salts. Based on recent reports, ~70% of the electrolytes applied in Bi-based PIBs are 1 M K dissolved in DME. Increasing the salt content results in enhanced interactions between cations and anions. Increasing the salt concentration also decreases the content of free-state solvent molecules. When the concentration is increased (>3 M), however, the free molecules decrease, leading to a change in the solution structure, which usually gives rise to extraordinary electrochemical properties and shifts the location of the LUMO from the solvent molecules to the salt. Thus, the reductive decomposition of salts takes place before the decomposition of the solvent, which results in the formation of a stable SEI^[69,72]. Zhang *et al.* first used a concentrated electrolyte in Bi-based PIBs^[73]. The Bi@C anode delivered the highest capacity of 202 mAh g⁻¹ in a 5 M KFSI-diethylene glycol dimethyl ether electrolyte, which was higher than those in 1 M (163 mAh g⁻¹), 3 M (153 mAh g⁻¹) and 7 M (93 mAh g⁻¹) electrolytes. Based on this study, the differences in the electrochemical performance were due to the

different reduction resistances. The decreased reduction resistance in the 5 M electrolyte depressed the irreversible electrochemical reaction and formed less SEI compared to the less concentrated electrolytes^[73]. A comparison of the electrochemical performance of Bi-based anode materials in PIBs is shown in [Table 2](#).

Based on the current study of Bi-based PIBs, KFSI-based electrolytes have better electrochemical performance compared to KPF₆-based electrolytes because of the higher ionic conductivity and the formation of a more stable and uniform SEI. Some ether-based electrolytes have extraordinary performance in half cells because their ether-derived SEI possesses better mechanical flexibility. The concentrated electrolyte can improve the electrochemical performance to a certain extent due to the lower resistance of the electrolyte.

Sb-based electrodes for PIBs

Antimony is a layered structure hexagonal element with a high electrical conductivity of $2.5 \times 10^6 \text{ S}\cdot\text{m}^{-1}$. Studies of Sb as anode applied in batteries can be traced back to the 1970s^[77] when Weppner first studied its kinetic parameters and thermodynamic properties in mixing conducting electrodes to be applied in a Li₃Sb system. Theoretically, one mole of Sb can alloy with three moles of lithium, sodium or potassium. The first study of Sb in PIBs was in 2015^[78]. Sb is a promising anode material with a high theoretical capacity of 687 mAh g⁻¹ in PIBs, which makes it a novel potential anode material.

K-ion storage mechanism of Sb

Based on the Sb-K phase diagram, there are four K-Sb binary phases going through K₃Sb, K₅Sb₄, KSb and K₂Sb₂ with decreasing K content^[79]. The corresponding equilibrium potentials of K₂Sb₂, KSb, K₅Sb₄ and K₃Sb are 0.890, 0.849, 0.439 and 0.398 V, respectively, based on DFT computations^[74], which are shown in [Figure 7A-C](#). *In-situ* XRD experiments and cyclic voltammetry (CV) were carried out to analyze the phase changes^[80]. In the discharge process, the first step was the transformation of hexagonal Sb to amorphous Sb. As reported, the peak at 28.6° corresponding to the (012) phase of Sb gradually became weaker^[81], as shown in [Figure 7D](#). In the amorphous region, K₂Sb₂ and KSb phases can form at the potential of 0.78 V and at the potential of 0.23 V, K₅Sb₄ phase can form based on the CV results. When fully discharged to ~0.2 V, the cubic K₃Sb phase with *Fm3m* symmetry forms as the final potassiation product. Upon charging, the K₃Sb phase gradually decreases by the formation of the intermediate phase K_xSb. When further charging, the Sb phase forms with the decomposition of intermediate K_xSb. In addition, the cubic K₃Sb phase can be observed in the second cycle, while no crystalline Sb can be observed^[82].

One interesting observation is the formation of the cubic K₃Sb phase as the fully discharged product. There are two polymorphs of K₃Sb, hexagonal K₃Sb (h-K₃Sb) and cubic K₃Sb (c-K₃Sb). Based on the DFT calculations, h-K₃Sb is more stable than c-K₃Sb, as shown in [Figure 7E](#)^[83]. If we consider the crystalline energy and the reaction activation energy, however, the results are different. The following equation represents the activation barrier $\Delta E^*(x)$:

$$\Delta E^*(x) = 16\pi\gamma^3/3(\Delta E_g(x)/\rho(x)V_0)^2. \quad (5)$$

where γ represents the surface energy, ΔE_g represents the energy gain on passing from the crystalline to amorphous phase and V_0 is the molar volume of the crystalline phase, as shown in [Figure 7E](#) and [F](#). Even the molar energy gain of h-K₃Sb is higher than that of c-K₃Sb by ~0.12 eV and h-K₃Sb also has a higher surface energy and lower density. As a result, h-K₃Sb has a higher activation barrier, which results in the final formation of c-K₃Sb instead of h-K₃Sb^[83]. Thus, based on current reports, the reaction can be concluded as $Sb_{crystal} \rightarrow Sb_{amorphous}$, $Sb_{amorphous} + xK^+ + xe^- \leftrightarrow K_xSb_{amorphous}$ and $K_xSb_{amorphous} + (3-x)K^+ + (3-x)e^- \leftrightarrow c-K_3Sb_{crystalline}$.

Table 2. Summary of electrochemical performance of Bi-based anodes for PIBs

Anode materials	Modification methods	Synthesis method	Redox potential (vs.K/K')	Current Density (mA g ⁻¹)	Initial capacity (potassiation) (mAh g ⁻¹)	Initial depotassiation (mAh g ⁻¹)	1st CE	Cycling performance	Best rate capability	Electrolyte	Ref.	
Bi/rGO	Bi/rGO	Hybridized with graphene	Simple room-temperature solution synthesis method	1.29 V 0.72-0.23 V	50	700	441	63%	Reversible capacity of 290 mAh g ⁻¹ after 50 cycles at current density of 50 mA g ⁻¹	290 mAh g ⁻¹ after 50 cycles at current density of 50 mA g ⁻¹	1 M KFSI in EC/DEC (1:1, v/v)	[59]
	Porous Bi	Nanostructural design	Commercial	0.93-0.30 V	2C	371.4	322	87.2%	After 300 cycles, the capacity remained at 282 mAh g ⁻¹	At 3C, the capacity is still high at up to 321.9 mAh g ⁻¹	1 M KPF ₆ in DME.	[58]
	Bi@3DGFs	Hybridized with 3D porous graphene/design of 2D nanostructure	Solid-state reaction	0.4-0.5 V 0.6-0.7 V	100	671	241	36%	185.2 mAh g ⁻¹ at 10 A g ⁻¹ after 2000 cycles	Rate capability of 180 mAh g ⁻¹ at 50 A g ⁻¹	1 M KPF ₆ in DME	[63]
	Bi-doped porous carbon	Hybridized with porous carbon/design of nanostructure	Wet chemistry/thermal treatment	/	200	656	382	58.2%		High capacity of 107 mAh g ⁻¹ at 20 A g ⁻¹	0.8 M KPF ₆ in EC/DEC	[64]
	Bi nanorod/carbon	Hybridized with carbon	Wet chemistry/thermal treatment	0.2-0.5 V	1000	723	470	65%	91% capacity retention at 5 A g ⁻¹ after 1000 cycles	289 mA h g ⁻¹ at current density of 6 A g ⁻¹	1 M KPF ₆ in DME	[74]
	Bi nanorod/N-doped carbon	Hybridized with carbon/design of nanostructure	Thermal method	0.3-0.5 V	385	450	316	70%	266 mA h g ⁻¹ over 1000 cycles at 10C	297 mA h g ⁻¹ at 20C	1 M KPF ₆ in DME	[66]
	Bi@N-doped carbon nanosheets	Hybridized with N-doped carbon/design of nanostructure	Wet chemistry/thermal treatment	0.3-0.5 V	1000	721	346	48%	180 mAh g ⁻¹ at 30 A g ⁻¹ after 1000 cycles	175 mAh g ⁻¹ at 30 A g ⁻¹	1 M KPF ₆ in DME	[65]
	Bi@N-doped carbon	Hybridized with N-doped carbon/design of nanostructure	Evaporation method	0.25-0.81 V	50	624	373	59.7%	179.1 mAh g ⁻¹ at 50 mA g ⁻¹ after 300 cycles	162 mA h g ⁻¹ at 1.5 A g ⁻¹	1 M KFSI in DME	[75]
	Multicore-shell Bi@N-C	Hybridized with Carbon/design of nanostructure	Solvothermal method/ Thermal treatment	0.77-0.32 V	1000	972	355	36.5%	235 mAh g ⁻¹ after 2000 cycles at 10 A g ⁻¹	152 mAh g ⁻¹ at 100 A g ⁻¹	1 M KPF ₆ in DME	[76]

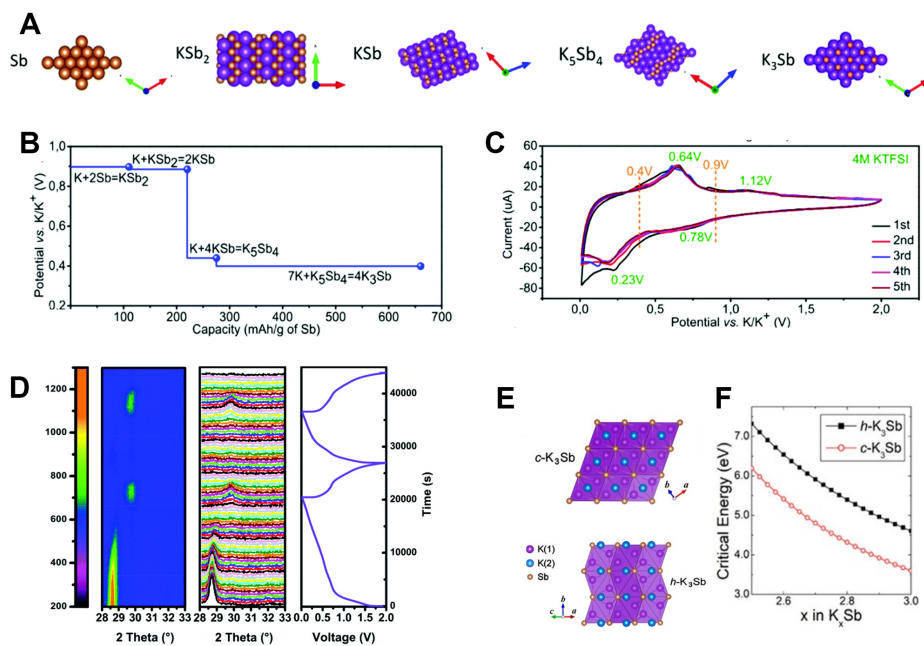


Figure 7. (A) Crystal structures of Sb and K-Sb binary phases. (B) DFT-calculated equilibrium voltages (vs. K/K^+) for potassiation process. (C) CV curves of Sb-based electrode at a scan rate of 0.05 mV s^{-1} . Copyright 2019, Royal Society of Chemistry. (D) *In-situ* XRD patterns of 3D Sb nanoparticle (NP)@C electrode during a potassiation/depotassiation/potassiation process at 100 mA g^{-1} and the corresponding discharge/charge curves. Copyright 2018, Royal Society of Chemistry. (E) Crystal structures of c- $K_3\text{Sb}$ and h- $K_3\text{Sb}$. (F) Critical energies for nucleation of $K_3\text{Sb}$ phase. Copyright 2019, American Chemistry Society.

The study of the potassiation mechanisms of Sb-based alloy compounds has also attracted significant attention. Liu *et al.* were the first to report the potassiation/depotassiation process of Sb_2S_3 .^[84] The process includes three steps. The first step is an intercalation reaction: $\text{Sb}_3\text{S}_3 + x\text{K}^+ + xe^- \rightarrow \text{K}_x\text{Sb}_2\text{S}_3$. The following two steps are the conversion-alloying reaction of $\text{Sb}_2\text{S}_3 + x\text{K}^+ + xe^- \leftrightarrow \gamma\text{K}_3\text{Sb} + z\text{K}_2\text{S}_3$. Their results showed no interaction process but only an alloying-conversion process with extra electron transfer. Sb_2Se_3 -based microtubes were prepared and analyzed by Yi *et al.*^[85] Based on their study, the potassium insertion reaction in the composite delivered a conversion-alloying reaction. The reaction process can be concluded to be $\text{Sb}_2\text{Se}_3 + 12\text{K}^+ + 12e^- \leftrightarrow 3\text{K}_3\text{Sb} + 2\text{K}_2\text{Se}_3$. The Sb_2Se_3 compound first reacted with potassium to form the K_2Se and Sb phases, which were further alloyed with potassium. In the reduction process, K_2Se can be observed as an intermediate phase, which is reconverted to form Sb_2Se_3 . The whole process is reversible.

As discussed above, Sb will alloy with K to form the K_3Sb phase as the final alloying product, while Sb-based compounds will first undergo a conversion reaction with a subsequent alloying reaction.

Modification strategies for Sb-based anode materials

As discussed above, Sb will form K_3Sb as the final product. Sb has a high theoretical capacity of 660 mAh g^{-1} . It also has a safe operation voltage and high conductivity, which makes it a promising anode material for PIBs. Sb suffers, however, from large volume changes during the K^+ insertion and extraction processes. To relieve the large volume changes of Sb and improve its electrochemical performance, various methods have been applied, such as the utilization of nanostructures and combination with carbon materials^[86-90].

Nanostructural engineering combined with carbon materials has been a widely practiced method to improve the electrochemical performance of Sb. Huang *et al.* designed a hybrid structure with Sb nanoparticles as yolk confined in a carbon box shell, which was prepared using metal-organic frameworks

as precursors^[86]. As observed by *in-situ* TEM, this hybrid material, which consists of carbon fibers with yolk-shell Sb@C, has structural advantages in the potassiation and depotassiation processes, as shown in Figure 8A-D. The inner Sb nanoparticles suffer from significant volume expansion during the potassiation process, while the void space effectively relieves the volume changes and the carbon fiber shell maintains the integrity of the structure and improves the conductivity. As a result, it delivered a capacity of 227 mAh g⁻¹ after 1000 cycles and had a high Coulombic efficiency of ~100%. Liu *et al.* designed and constructed Sb nanoparticles confined by carbon, which exhibited long cycling stability over 800 cycles with a capacity retention as high as 72.3%^[87], as shown in Figure 8E.

A variety of porous structures have been applied to hinder the volume change during cycling^[88-91]. A microsized nanoporous antimony potassium anode was designed with tunable porosity^[88]. The nanoporous structure can accommodate volume expansion and accelerate ion transport. Similarly, Zhao also encapsulated Sb nanoparticles within a porous architecture^[89]. The composite delivered a high capacity of 392.2 mAh g⁻¹ at 0.1 A g⁻¹ after 450 cycles. Carbon nanofibers have also been applied as nanochannels to solve the issues of poor potassium-ion diffusion and significant volume variation. The Sb@CNFs delivered a reversible capacity of 225 mAh g⁻¹ after 2000 cycles^[90]. Cheng *et al.* utilized a single-crystal nanowire structure to improve the electrochemical performance of a Sb₂S₃ anode material^[91]. After full potassiation, no obviously pulverization was observed, although the diameter of the as-prepared Sb₂S₃@C nanowires increased from 83 to 120 nm with a 45% expansion. The overall expansion of Sb₂S₃@C is ~111%, which is lower than the Sn-K alloying reaction ($\approx 197\%$), indicating that the nanowire structure can effectively hinder the volume change during the potassiation/depotassiation process. Similarly, Jiao and Yu^[92,93] also utilized a one-dimensional structure. A 2D structure was also applied to improve the electrochemical performance of Sb-based anode materials. Wang *et al.* designed a Sb₂S₃ nanoflower/MXene composite that exhibited a high reversible capacity of 461 mAh g⁻¹ at a current density of 100 mA g⁻¹^[94]. Its structural stability was enhanced by the strong interfacial connection between Sb₂S₃ and the matrix. A 3D structure was also applied in Sb-based anode materials. A core-shell Sb@Sb₂O₃ heterostructure was fabricated, which delivered an excellent capacity of 239 mAh g⁻¹ at 5 A g⁻¹ in PIBs^[95]. These methods efficiently improved the electrochemical performance of Sb-based anode materials.

Another important method is improving the binder for the electrodes. He *et al.* used a polyvinylidene fluoride (PVDF) binder, which has a high capacity of 226 mAh g⁻¹ over 400 cycles^[96]. Compared to PVDF, sodium carboxymethyl cellulose (CMC) can improve the initial columbic efficiency due to the pre-formed SEI. In addition to these traditional binders applied in PIBs, the group of Guo developed a CMC-polyacrylic acid (PAA) binder for a Sb-based composite^[97]. The cycling performance of the CMC-PAA binder was improved due to the condensation reaction between the hydroxyl groups of CMC and the carboxylic acid moieties of PAA, which effectively increased the viscoelastic properties of the binder and increased the mechanism properties of the electrodes.

In summary, the modification methods for Sb-based anode materials are mainly nanostructural engineering by designing nanofibers, nanoflowers, box shell structures and nanoporous structures in combination with carbon fibers, MXenes, carbon shells, and so on. Multistructural design efficiently hinders the significant volume change and efficiently alleviates the structural degradation.

Ge-based anode materials

Ge has a diamond cubic crystal structure, which is the same as silicon, and it is in the IVA group. Germanium is an attractive non-toxic alloy-based anode material. The original study of Ge-based anode materials can be dated back to the 1980s when the formation of the Ge-Li binary was first discovered.

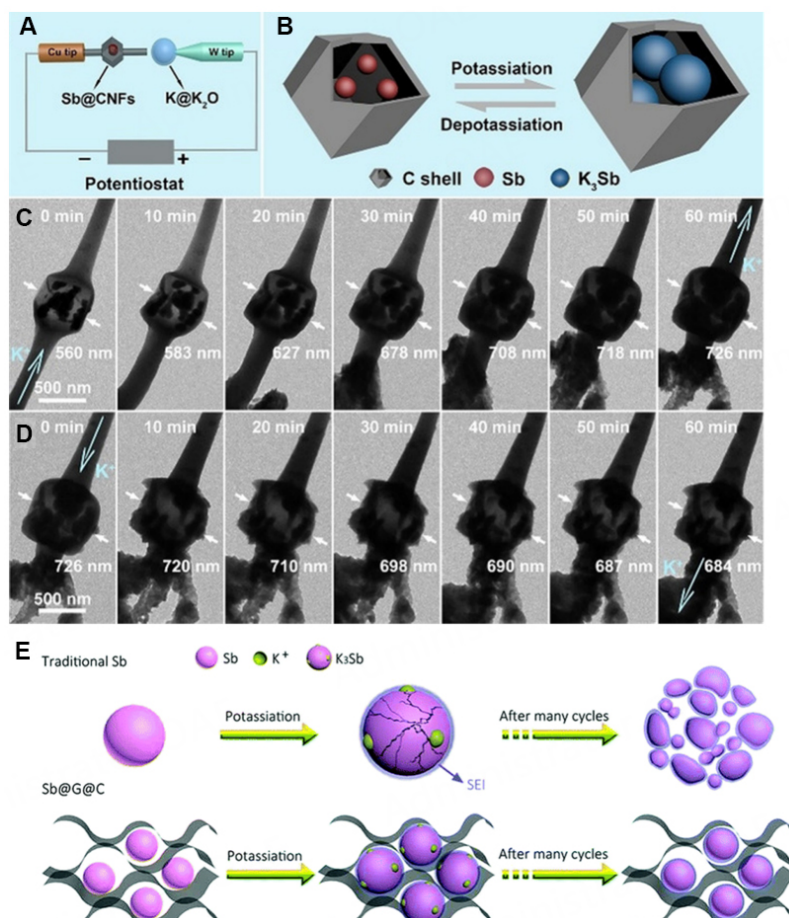


Figure 8. (A) Illustration of TEM device and (B) potassiation/depotassiation processes of Sb@carbon nanofibers (CNFs) with Sb nanoparticles confined in carbon shell. (C and D) Potassiation and depotassiation processes of Sb@CNFs^[86]. Copyright 2020, Wiley-VCH. (E) Schematic illustration of traditional Sb and Sb@graphene (G)@C electrodes during potassiation/depotassiation processes^[87]. Copyright 2018, Royal Society of Chemistry.

Mechanism of Ge-based anodes in PIBs

Ge has a high capacity of 1623 or 1384 mAh g⁻¹ by the formation of the lithium-rich compounds Li₅Ge₃ and Li₁₅Ge₄, respectively^[98-102], which makes it a promising anode material in LIBs. In SIBs, germanium delivers a high capacity of 389 mAh g⁻¹ by forming the binary compound NaGe^[103-106] at a voltage plateau of 0.15-0.60 V vs. Na/Na⁺. Based on the formation of KGe as the final product, germanium has a theoretical capacity of 369 mAh g⁻¹ in PIBs. To date, the study of the potassium-ion storage mechanism for Ge in PIBs has been limited. Based on the previous studies of the performance of Ge in SIBs and LIBs, the mechanism of potassium-ion insertion obeys the following equation: $Ge + K^+ + e^- \leftrightarrow KGe$. This mechanism was proved using SAED^[107]. For Ge-based compounds, the mechanism can be simplified to $Ge_xM_y + (x + zy)K^+ + (x + zy)e^- = xKGe + yK_zM^{[42]}$. In this process, the compound first decomposes, the Ge reacts with K to form KGe and the active material reacts with K to form a compound. When the Ge-based compounds are 2D materials, such as GeSe, the reaction can be considered as $GeSe + xK^+ + xe^- \leftrightarrow K_xGeSe$ based on calculations^[108,109].

Modification strategies for Ge-based anode materials

Compared to other alloy-based anode materials, germanium has a relatively lower theoretical capacity. It experiences a limited volume change during ion insertion and extraction processes; however, compared to

other alloy-based anodes, which amount to ~272% in LIBs and 120% in SIBs. Similarly, Ge undergoes a significant volume change in the discharge/charge process in PIBs. Although the volume changes of germanium are less compared to other alloy-based materials, they can cause pulverization and result in a capacity decrease in the same manner.

In order to improve the electrochemical performance of germanium-based anode materials, the ordinary methods include constructing nanostructures combining Ge with carbon materials^[110-114] in LIBs and SIBs. Li *et al.* designed hollow carbon spheres with germanium encapsulated inside by introducing a germanium precursor into the hollow carbon particles and then followed this with a thermal reduction^[114]. The hollow carbon spheres served as a physical matrix that could effectively protect the germanium core from coalescing or pulverization. Similarly, Mo *et al.* designed a 3D-interconnected porous graphene foam with germanium quantum dots doped into it by a facile approach^[112]. This structure provided close contact between the electrode materials and the current collector, and the yolk-shell structure effectively alleviated the significant volume changes and provided a stable SEI. Designing nanostructures in combination with carbon materials are also an efficient method to improve the electrochemical performance of Ge-based materials in PIBs. Liu *et al.* synthesized a dual carbon structure with germanium encapsulated inside^[106]. The as-prepared dual carbon matrix was composed of mesoporous carbon and an amorphous carbon layer, as shown in Figure 9. Using this structure, the dual carbon effectively alleviated the expansion of germanium. Yang *et al.* designed a nanoporous structure Ge with small ligaments and interconnected porous prepared by a chemical-dealloying method^[107]. The nanoporous germanium delivered a high initial capacity of 290 mAh g⁻¹ and a stable capacity of 120 mAh g⁻¹ over 400 cycles^[107].

Using active or inactive elements to form Ge-based binaries or composites is another effective method to improve the electrochemical performance. The inactive metals alloyed with Ge include Co^[115] and Cu^[116], which can improve the conductivity. The active materials have been applied in the formation of Ge-based compounds are Si^[117], Sn^[118], Sb^[119], Te^[120] and Se^[121], which have high theoretical capacities. As discussed above, phosphorus has the highest theoretical capacity in PIBs and can increase the capacity of the total capacity by the formation of GeP_x. Zhang *et al.* prepared GeP₅, which delivered a stable capacity of 213.7 mAh g⁻¹ in PIBs for 2000 cycles at a current density of 500 mA g⁻¹^[51]. The active Se metal can form layered metal selenides with Ge, which has a large interlayer distance of 5.41 Å. The GeSe/CNT composite synthesized by a simple ball-milling method delivered a stable cycling performance with 311 mAh g⁻¹ retention after 400 cycles. Furthermore, the electrode delivered a capacity of ~200 mAh g⁻¹ at a high current density of 5 A g⁻¹^[122]. Ge-based anode materials exhibit larger volume changes in PIBs compared to the volume changes in LIBs and SIBs because of the larger size of potassium ions. The construction of 3D porous and yolk-shell structures in combination with carbon materials, such as carbon spheres, graphene or amorphous carbon, can efficiently ameliorate the volume changes and improve the electrochemical performance.

Sn-based anode materials for PIBs

Sn has been an attractive anode material for LIBs and SIBs for a long time and has high theoretical capacities of 991 and 845 mAh g⁻¹ via the formation of Li_{4.4}Sn and Na₁₅Sn₄, respectively. The study of Sn in PIBs started in 2016^[123], with the formation of KSn. Sn has a theoretical capacity of 226 mAh g⁻¹ in PIBs.

Mechanism of Sn-based anode materials

Based on the K-Sn phase diagram, K₂Sn, KSn, K₂Sn₃, KSn₂ and K₄Sn₂₃ can form at different temperatures. Wang *et al.* were the first to study the reaction mechanism of Sn in PIBs using *in-situ* TEM and XRD methods^[124]. They revealed a two-step process corresponding to Sn → amorphous K₄Sn₉ → KSn. A similar

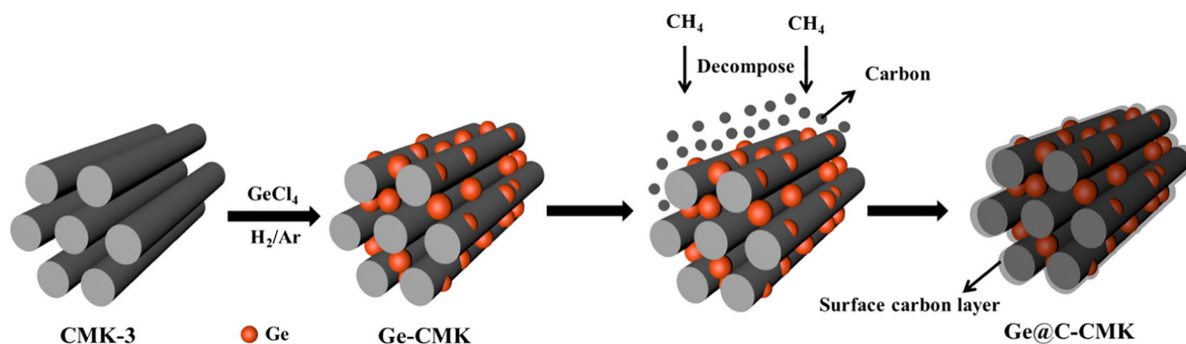


Figure 9. Schematic illustration of preparation of Ge-CMK and Ge@C-CMK composites^[106]. Copyright 2021, Elsevier.

potassiation process was evaluated, as shown in Figure 10A-C. The results revealed that the tetragonal K_4Sn_4 phase was formed at a voltage of ~ 0.01 V. Their study indicated that K_4Sn_4 and KSn are overall identical phases in terms of their crystal structure. In the de-alloying process, K_4Sn_4 decomposed at 0.98 V^[125].

The study of the mechanism of Sn-based alloys has also attracted significant attention. The teams of Ma and Ci have both studied the potassium-ion storage mechanism in SnS_2 ^[126,127] and their results are similar. In the discharge process, $SnS_2 \rightarrow SnS + K_2S_5 \rightarrow Sn + K_2S_5 + K_4Sn_{23} \rightarrow K_2S_5 + KSn$, as shown in Figure 10D. Like the alloying process of crystalline Sn in PIBs, the final product, KSn phase, is formed within the voltage range of 0.20 - 0.01 V. For $SnSe$, based on the study of Verma *et al.*, the potassiation process is $SnSe \rightarrow Sn + K_2Se_5 \rightarrow K_4Sn_{23} + K_2Se_5$, which is reversible^[128]. The KSn phase was not detected, as shown in Figure 10E.

Modification strategies for Sn-based anode materials

Sn-based alloys suffer from significant volume expansion in PIBs, which results in pulverization and capacity drop. Various methods have been applied to ameliorate the volume change and improve the electrochemical performance. To solve these drawbacks, hierarchical nanostructural design is an effective strategy. 2D nanosheet structures have been applied to improve the electrochemical performance of Sn-based anode materials. Lakshimi *et al.* studied an SnS_2 /graphene composite in PIBs, which delivered a high capacity of 350 mAh g^{-1} ^[129]. Qin *et al.* designed hierarchical polyaspartic acid-modified SnS_2 nanosheets embedded into carbon^[126]. The as-prepared electrode enlarged the interlamellar space of 6.8 Å and delivered a high-rate performance of 273 mAh g^{-1} at a current density of 2 A g^{-1} ^[126]. Cao *et al.* also designed a 2D SnS nanosheet composite that exhibited an ultralong lifespan^[130]. Sun *et al.* used a nanosheet structure with strong interactions between the layers, which can efficiently accelerate electron and ion transfer and hinder the volume change^[131]. The as-prepared composite delivered a stable long-term cycling performance of 165 mAh g^{-1} at a current density of 10 A g^{-1} after 5000 cycles^[131].

The group of Yang also designed a nanosheet structure, which delivered a high capacity of 206.1 mAh g^{-1} after 800 cycles^[132]. Zhou *et al.* designed a sheet-like tin sulfide composite, as shown in Figure 11A, which delivered a rapid rate capacity of 460 mAh g^{-1} at a current density of 2 A g^{-1} and an excellent cycling stability of over 500 cycles at a current density of 1 A g^{-1} ^[133]. The utilization of the 2D structure efficiently hinders the volume change and improves the electronic and ionic conductivity. Combining Sb-based alloys with 3D structures has been an effective method to improve the electrochemical performance of PIBs. Yolk-shell 3D carbon boxes were designed as a matrix to accommodate SnS_2 , as shown in Figure 11B. Introducing interior void space has been an effective strategy to accommodate the volume changes. The composite delivered a stable cycling performance of 352 mAh g^{-1} at 1 A g^{-1} , as shown in Figure 11C^[134].

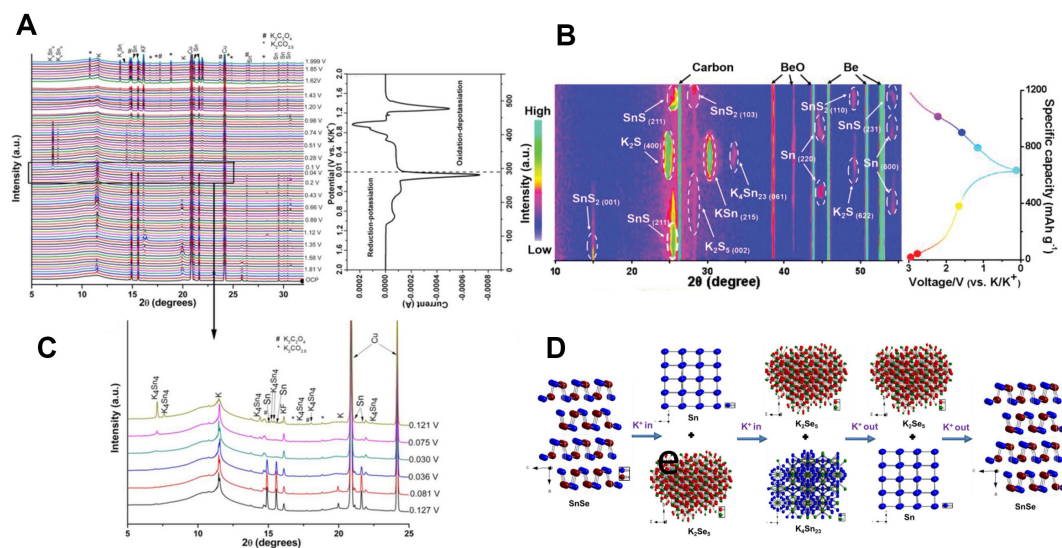


Figure 10. (A) Synchrotron XRD data obtained *in situ* during (B) CV scans of 1 μm -thick Sn film electrode in K half-cell and (C) zoomed-in *in-situ* XRD patterns corresponding to region associated with phase transformation of primary interest during electrochemical potassiation of Sn^[125]. Copyright 2017, Electrochemical Society. (D) *In-situ* XRD results for hierarchical polyaspartic acid-modified SnS₂ nanosheets embedded into hollow N-doped carbon fibers (PASP@SnS₂@CN) electrode at different charge/discharge states^[126]. Copyright 2020, Wiley-VCH. (E) Schematic illustration of potassiation/depotassiation process in SnSe@C nanocomposite^[128]. Copyright 2021, Elsevier Ltd.

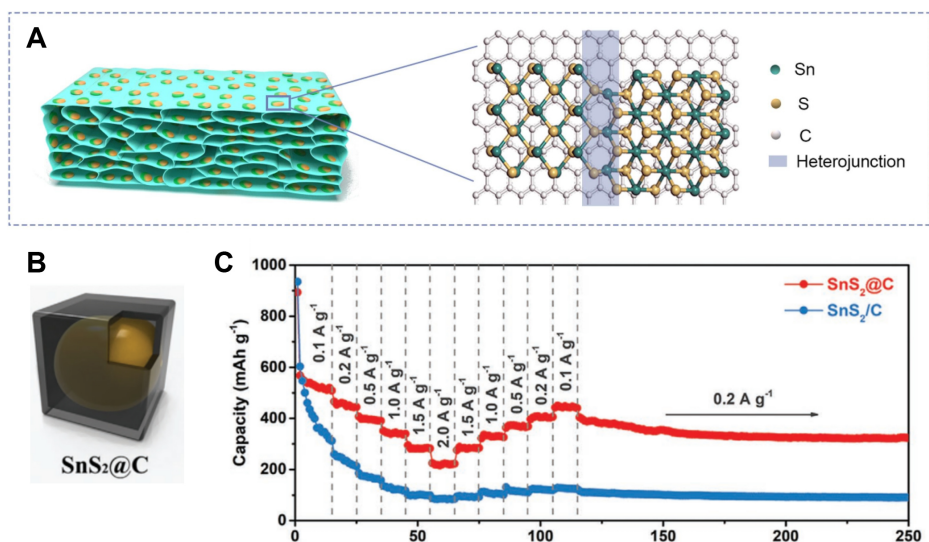


Figure 11. (A) Morphological and structural characterization of SnS/SnS₂/rGO materials^[133]. Copyright 2021, Elsevier Ltd. (B) Schematic illustration of SnS₂@C and (C) long-term cycling stability evaluation of SnS₂@C and SnS₂/C electrodes in PIBs^[134]. Copyright 2020, Wiley-VCH.

Another alternative method to enhance electrochemical performance is using the proper salt to form a robust SEI. Compared KFSI and KPF₆ with the same solvent. The results indicated that the Sn-based composite in the KFSI-based electrolyte exhibited a highly stable cycling performance of 450 mAh g⁻¹ over 400 cycles. The KFSI salt in an ethylene carbonate/diethyl carbonate solvent more easily forms a K-F-rich inorganic SEI due to the critical role of FSI⁻¹ anions, which can inhibit the decomposition of the electrolyte^[135], as shown in Figure 12A. Similarly, the group of Chen also studied the different salts in

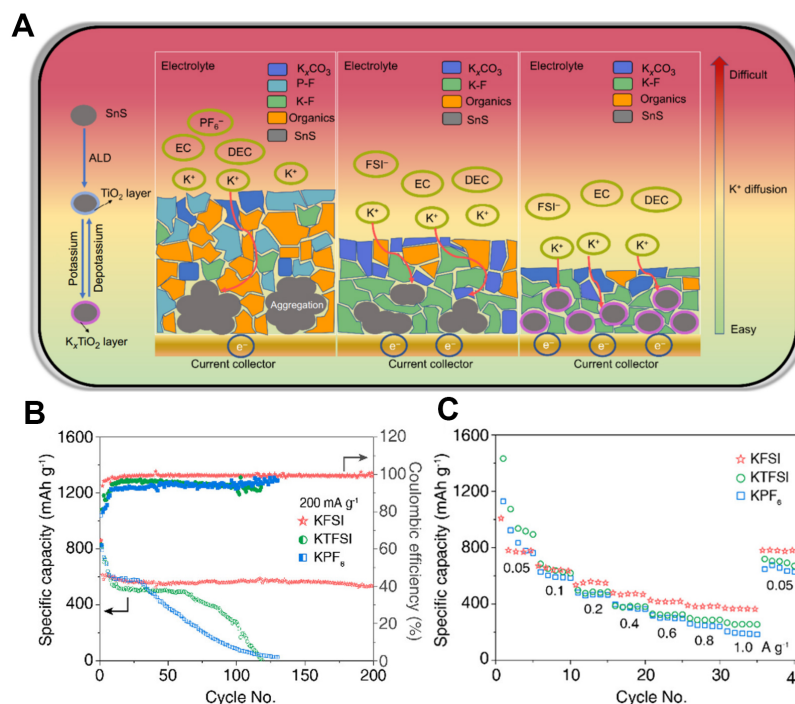


Figure 12. (A) Schematic illustration of chemical composition and ionic transport of electrode/electrolyte interface^[135]. Copyright 2021, Springer Nature. (B) Capacity retention of SnS₂/N-rGO composite electrodes in EC/DEC electrolytes with various K⁺ salts at a current density of 200 mA g⁻¹. (C) Rate capability of cells with various K⁺ salts at current densities from 0.05 to 1 A g⁻¹^[136]. Copyright 2021, American Chemical Society.

electrolytes resulting in the differences in SEI formations. Their results indicated that batteries with KFSI featured better performance than those with KTFSI and KPF₆. The composition of the SEI formed in the KFSI-based electrolyte is mainly K-F, which can effectively enhance the mechanical properties of the SEI. The SEI from the KFSI-based electrolyte also stops growing after 20 cycles, while the SEIs of the KTFSI and KPF₆-based electrolytes continue to grow thicker, thereby hindering the potassium-ion transportation, as shown in Figure 12B and C^[136]. Sn has a high theoretical capacity of 226 mAh g⁻¹ in PIBs, with the formation of KSn as the final product. The challenge facing Sn-based alloy anode materials in PIBs is their significant volume change and pulverization. In order to hinder the volume change of Sn-based alloys, modification methods have been applied. The design of 2D nanosheets, 3D nanoboxes and SEIs has been applied in the modification and has efficiently improved the electrochemical performance.

SUMMARY AND OUTLOOK

Their low cost and the natural abundance of their raw materials make PIBs promising next-generation energy storage devices. The large radius of the potassium ion results, however, in slower ion transport and limited cycling life. Recently, significant research has been completed on PIBs, but one of the major challenges is to develop high-performing anodes.

This review summarizes the recent research progress on alloy-type anodes for PIBs, including P-, Bi-, Sb-, Ge- and Sn-based compounds and composites. Alloy-based anode materials undergo alloy conversion reactions in which the material finally reacts with K to form K_xM. Therefore, alloy-based materials have high theoretical capacities of 2596, 385, 687, 369 and 226 mAh g⁻¹, respectively, and volumetric capacities of 4750, 3752, 4596, 1964 and 1653 mAh cm⁻³ make them high potential anode materials for PIBs. The

mechanisms of the potassiation and depotassiation processes have been deeply discussed and analyzed. For an elementary substance, the mechanism is a simple alloying reaction. For compound materials, the reaction process is mainly a conversion-alloying reaction. The various formations of the intermediate product in the potassium ion for the same material are mainly due to the various nanostructures and grain sizes of the materials. Modifications of the materials have also been explored and investigated. The approaches can be classified as the hybridization of active materials with high conductivity and architectural engineering. Highly conductive materials, including graphene, carbon nanotubes, graphite, N-doped carbon and carbon nanosheets. The architectural engineering methods, including the design of one-dimensional nanotubes, 2D nanosheets and 3D structural materials, such as core-shell structures and their combinations. By using these modification methods, the significant volume change and sluggish reaction kinetics can be effectively solved.

The electrochemical performance of alloy-based electrodes has now been greatly improved and the reaction processes have also been deeply analyzed. Further research can be carried out on the following aspects:

(1) Low initial Coulombic efficiency is the main problem that remains for anode materials, which might be ascribed to the irreversible insertion of potassium ions and the decomposition of the electrolyte. In the full cell, the maximum cell energy is obtained when the anode irreversible capacity exactly matches that of the cathode material. The low initial Coulombic efficiency (ICE) indicates the large consumption of K^+ provided from cathode, which results in lower energy density in the full cell and faster capacity drop. Improving electrolytes with higher ion conductivity will increase the ICE.

(2) Although fabricated nanostructures and hybrids with carbon will significantly hinder the volume changes, alloy-based anode materials still face the problem of volume expansion and pulverization during cycling. Furthermore, this problem may bring the severe side effect of the reaction between the electrolyte and the new surface of the electrode, leading to the formation of the SEI on the new surface, which results in a capacity decrease and instability of the cycling performance. This side effect may also result in the maldistribution of electrons, leading to dendrite growth and the polarization of electrodes. This will limit the application and manufacturing of PIBs. Electrolyte and electrode interface engineering or controlling the content and structure of the SEI layer or designing an artificial SEI layer can make up for the shortage.

(3) Safety problems are still an issue for future development. Alloy-based anode materials are currently limited in their application at high and low temperatures. Aqueous electrolyte and flame-retardant electrolyte systems could be promising designs for future applications. In addition, non-flammable carbonate electrolytes can also be used to address battery safety issues.

In light of the abundance of potassium resources and the significant progress that has been made in the research on alloy-based anodes for PIBs, these anodes will be promising for commercialization in the near future.

DECLARATIONS

Acknowledgments

The authors thank Dr. Tania Silver for her critical reading of the manuscript.

Authors' contributions

Characterizing, writing original draft: Yang Q

Review, and supervision: Chou S, Liu H, Wang J

Editing: Fan Q, Peng J

Availability of data and materials

Not applicable.

Financial support and sponsorship

This work is financially supported by Australian Research Council (ARC) Discovery Project (DP180101453).

Conflicts of interest

All authors declared that there are no conflicts of interest.

Ethical approval and consent to participate

Not applicable.

Consent for publication

Not applicable.

Copyright

© The Author(s) 2023.

REFERENCES

1. Scott V, Haszeldine RS, Tett SFB, Oschlies A. Fossil fuels in a trillion tonne world. *Nat Clim Chang* 2015;5:419-23. DOI
2. Mohr S, Wang J, Ellem G, Ward J, Giurco D. Projection of world fossil fuels by country. *Fuel* 2015;141:120-35. DOI
3. Abas N, Kalair A, Khan N. Review of fossil fuels and future energy technologies. *Futures* 2015;69:31-49. DOI
4. Höök M, Tang X. Depletion of fossil fuels and anthropogenic climate change - A review. *Energy Policy* 2013;52:797-809. DOI
5. Armaroli N, Balzani V. The legacy of fossil fuels. *Chem Asian J* 2011;6:768-84. DOI PubMed
6. Berner RA. The long-term carbon cycle, fossil fuels and atmospheric composition. *Nature* 2003;426:323-6. DOI PubMed
7. Gustavsson L, Börjesson P, Johansson B, Svaningsson P. Reducing CO₂ emissions by substituting biomass for fossil fuels. *Energy* 1995;20:1097-113. DOI
8. Withagen C. Pollution and exhaustibility of fossil fuels. *Resour Energy Econ* 1994;16:235-42. DOI
9. Barbir F, Veziroğlu T, Plass H. Environmental damage due to fossil fuels use. *Int J Hydrog Energy* 1990;15:739-49. DOI
10. Hameer S, van Niekerk JL. A review of large-scale electrical energy storage: this paper gives a broad overview of the plethora of energy storage. *Int J Energy Res* 2015;39:1179-95. DOI
11. Castillo A, Gayme DF. Grid-scale energy storage applications in renewable energy integration: a survey. *Energy Convers Manag* 2014;87:885-94. DOI
12. Etacheri V, Marom R, Elazari R, Salitra G, Aurbach D. Challenges in the development of advanced Li-ion batteries: a review. *Energy Environ Sci* 2011;4:3243. DOI
13. Hosaka T, Kubota K, Hameed AS, Komaba S. Research development on K-ion batteries. *Chem Rev* 2020;120:6358-466. DOI
14. Kim H, Kim JC, Bianchini M, Seo D, Rodriguez-garcia J, Ceder G. Recent progress and perspective in electrode materials for K-ion batteries. *Adv Energy Mater* 2018;8:1702384. DOI
15. Hwang J, Myung S, Sun Y. Recent progress in rechargeable potassium batteries. *Adv Funct Mater* 2018;28:1802938. DOI
16. Anoopkumar V, John B, Mercy T. Potassium-ion batteries: key to future large-scale energy storage? *ACS Appl Energy Mater* 2020;3:9478-92. DOI
17. Zhang W, Liu Y, Guo Z. Approaching high-performance potassium-ion batteries via advanced design strategies and engineering. *Sci Adv* 2019;5:eaav7412. DOI PubMed PMC
18. Li W, Bi Z, Zhang W, et al. Advanced cathodes for potassium-ion batteries with layered transition metal oxides: a review. *J Mater Chem A* 2021;9:8221-47. DOI
19. Zhang X, Wei Z, Dinh KN, et al. Layered oxide cathode for potassium-ion battery: recent progress and prospective. *Small* 2020;16:e2002700. DOI PubMed
20. Eftekhari A. Potassium secondary cell based on Prussian blue cathode. *J Power Sources* 2004;126:221-8. DOI
21. Li L, Hu Z, Liu Q, Wang J, Guo Z, Liu H. Cathode materials for high-performance potassium-ion batteries. *Cell Rep Phys Sci* 2021;2:100657. DOI

22. Li L, Hu Z, Lu Y, et al. A low-strain potassium-rich prussian blue analogue cathode for high power potassium-ion batteries. *Angew Chem Int Ed* 2021;60:13050-6. DOI PubMed
23. Qin M, Ren W, Meng J, et al. Realizing superior prussian blue positive electrode for potassium storage via ultrathin nanosheet assembly. *ACS Sustain Chem Eng* 2019;7:11564-70. DOI
24. Liu S, Kang L, Jun SC. Challenges and strategies toward cathode materials for rechargeable potassium-ion batteries. *Adv Mater* 2021;33:e2004689. DOI PubMed
25. Yang Y, Zhou J, Wang L, et al. Prussian blue and its analogues as cathode materials for Na-, K-, Mg-, Ca-, Zn- and Al-ion batteries. *Nano Energy* 2022;99:107424. DOI
26. Min X, Xiao J, Fang M, et al. Potassium-ion batteries: outlook on present and future technologies. *Energy Environ Sci* 2021;14:2186-243. DOI
27. Zhang K, Gu Z, Ang EH, et al. Advanced polyanionic electrode materials for potassium-ion batteries: Progresses, challenges and application prospects. *Mater Today* 2022;54:189-201. DOI
28. Jian Z, Luo W, Ji X. Carbon electrodes for K-ion batteries. *J Am Chem Soc* 2015;137:11566-9. DOI PubMed
29. Luo W, Wan J, Ozdemir B, et al. Potassium ion batteries with graphitic materials. *Nano Lett* 2015;15:7671-7. DOI PubMed
30. Zhan F, Wang H, He Q, et al. Metal-organic frameworks and their derivatives for metal-ion (Li, Na, K and Zn) hybrid capacitors. *Chem Sci* 2022;13:11981-2015. DOI PubMed PMC
31. Liu S, Kang L, Zhang J, Jung E, Lee S, Jun SC. Structural engineering and surface modification of MOF-derived cobalt-based hybrid nanosheets for flexible solid-state supercapacitors. *Energy Stor Mater* 2020;32:167-77. DOI
32. Tu J, Tong H, Zeng X, et al. Modification of porous N-doped carbon with sulfonic acid toward high-ICE/capacity anode material for potassium-ion batteries. *Adv Funct Mater* 2022;32:2204991. DOI
33. Tian S, Zhang Y, Yang C, Tie S, Nan J. Nitrogen-doped carbon nanosheet coated multilayer graphite as stabilized anode material of potassium-ion batteries with high performances. *Electrochim Acta* 2021;380:138254. DOI
34. Sultana I, Rahman MM, Chen Y, Glushenkov AM. Potassium-ion battery anode materials operating through the alloying-dealloying reaction mechanism. *Adv Funct Mater* 2018;28:1703857. DOI
35. Komaba S, Hasegawa T, Dahbi M, Kubota K. Potassium intercalation into graphite to realize high-voltage/high-power potassium-ion batteries and potassium-ion capacitors. *Electrochem Commun* 2015;60:172-5. DOI
36. Cao K, Liu H, Li W, et al. CuO nanoplates for high-performance potassium-ion batteries. *Small* 2019;15:e1901775. DOI PubMed
37. Sultana I, Rahman MM, Ramireddy T, Chen Y, Glushenkov AM. High capacity potassium-ion battery anodes based on black phosphorus. *J Mater Chem A* 2017;5:23506-12. DOI
38. Jin H, Wang H, Qi Z, et al. A black phosphorus-graphite composite anode for Li-/Na-/K-ion batteries. *Angew Chem Int Ed* 2020;59:2318-22. DOI PubMed
39. Xiong P, Bai P, Tu S, et al. Red phosphorus nanoparticle@3D interconnected carbon nanosheet framework composite for potassium-ion battery anodes. *Small* 2018;14:e1802140. DOI PubMed
40. Wu Y, Hu S, Xu R, et al. Boosting potassium-ion battery performance by encapsulating red phosphorus in free-standing nitrogen-doped porous hollow carbon nanofibers. *Nano Lett* 2019;19:1351-8. DOI PubMed
41. Liu D, Huang X, Qu D, et al. Confined phosphorus in carbon nanotube-backboned mesoporous carbon as superior anode material for sodium/potassium-ion batteries. *Nano Energy* 2018;52:1-10. DOI
42. Zhang W, Mao J, Li S, Chen Z, Guo Z. Phosphorus-based alloy materials for advanced potassium-ion battery anode. *J Am Chem Soc* 2017;139:3316-9. DOI
43. Zhang W, Wu Z, Zhang J, et al. Unraveling the effect of salt chemistry on long-durability high-phosphorus-concentration anode for potassium ion batteries. *Nano Energy* 2018;53:967-74. DOI
44. Li B, He Z, Zhao J, Liu W, Feng Y, Song J. Advanced $\text{Se}_3\text{P}_4@\text{C}$ anode with exceptional cycling life for high performance potassium-ion batteries. *Small* 2020;16:e1906595. DOI
45. Yang Q, Tai Z, Xia Q, et al. Copper phosphide as a promising anode material for potassium-ion batteries. *J Mater Chem A* 2021;9:8378-85. DOI
46. Xu GL, Chen Z, Zhong GM, et al. Nanostructured black phosphorus/ketjenblack-multiwalled carbon nanotubes composite as high performance anode material for sodium-ion batteries. *Nano Lett* 2016;16:3955-65. DOI PubMed
47. Yang W, Lu Y, Zhao C, Liu H. First-principles study of black phosphorus as anode material for rechargeable potassium-ion batteries. *Electron Mater Lett* 2020;16:89-98. DOI
48. Yuan D, Cheng J, Qu G, et al. Amorphous red phosphorous embedded in carbon nanotubes scaffold as promising anode materials for lithium-ion batteries. *J Power Sources* 2016;301:131-7. DOI
49. Ramireddy T, Xing T, Rahman MM, et al. Phosphorus-carbon nanocomposite anodes for lithium-ion and sodium-ion batteries. *J Mater Chem A* 2015;3:5572-84. DOI
50. Verma R, Didwal PN, Ki HS, Cao G, Park CJ. $\text{SnP}_3/\text{Carbon}$ nanocomposite as an anode material for potassium-ion batteries. *ACS Appl Mater Interfaces* 2019;11:26976-84. DOI PubMed
51. Zhang Z, Wu C, Chen Z, et al. Spatially confined synthesis of a flexible and hierarchically porous three-dimensional graphene/FeP hollow nanosphere composite anode for highly efficient and ultrastable potassium ion storage. *J Mater Chem A* 2020;8:3369-78. DOI
52. Yang F, Gao H, Hao J, et al. Yolk-shell structured FeP@C nanoboxes as advanced anode materials for rechargeable lithium-/potassium-ion batteries. *Adv Funct Mater* 2019;29:1808291. DOI

53. Yang F, Hao J, Long J, et al. Achieving high-performance metal phosphide anode for potassium ion batteries via concentrated electrolyte chemistry. *Adv Energy Mater* 2021;11:2003346. DOI
54. Liu Q, Hu Z, Liang Y, et al. Facile synthesis of hierarchical hollow CoP@C composites with superior performance for sodium and potassium storage. *Angew Chem* 2020;132:5197-202. DOI PubMed
55. Li D, Zhang Y, Sun Q, et al. Hierarchically porous carbon supported Sn_4P_3 as a superior anode material for potassium-ion batteries. *Energy Stor Mater* 2019;23:367-74. DOI
56. Zhang W, Pang WK, Sencadas V, Guo Z. Understanding high-energy-density Sn_4P_3 anodes for potassium-ion batteries. *Joule* 2018;2:1534-47. DOI
57. Huang J, Lin X, Tan H, Zhang B. Bismuth microparticles as advanced anodes for potassium-ion battery. *Adv Energy Mater* 2018;8:1703496. DOI
58. Lei K, Wang C, Liu L, et al. A porous network of bismuth used as the anode material for high-energy-density potassium-ion batteries. *Angew Chem* 2018;130:4777-81. DOI PubMed
59. Zhang Q, Mao J, Pang WK, et al. Boosting the potassium storage performance of alloy-based anode materials via electrolyte salt chemistry. *Adv Energy Mater* 2018;8:1703288. DOI
60. Xie F, Zhang L, Chen B, et al. Revealing the origin of improved reversible capacity of dual-shell bismuth boxes anode for potassium-ion batteries. *Matter* 2019;1:1681-93. DOI
61. Shen C, Song G, Zhu X, et al. An in-depth study of heteroatom boosted anode for potassium-ion batteries. *Nano Energy* 2020;78:105294. DOI
62. Chen K, Chong S, Yuan L, Yang Y, Tuan H. Conversion-alloying dual mechanism anode: Nitrogen-doped carbon-coated Bi_2Se_3 wrapped with graphene for superior potassium-ion storage. *Energy Stor Mater* 2021;39:239-49. DOI
63. Cheng X, Li D, Wu Y, Xu R, Yu Y. Bismuth nanospheres embedded in three-dimensional (3D) porous graphene frameworks as high performance anodes for sodium- and potassium-ion batteries. *J Mater Chem A* 2019;7:4913-21. DOI
64. Hu X, Liu Y, Chen J, Yi L, Zhan H, Wen Z. Fast redox kinetics in Bi-heteroatom doped 3D porous carbon nanosheets for high-performance hybrid potassium-ion battery capacitors. *Adv Energy Mater* 2019;9:1901533. DOI
65. Shi X, Zhang J, Yao Q, et al. A self-template approach to synthesize multicore-shell Bi@N-doped carbon nanosheets with interior void space for high-rate and ultrastable potassium storage. *J Mater Chem A* 2020;8:8002-9. DOI
66. Li H, Zhao C, Yin Y, et al. N-doped carbon coated bismuth nanorods with a hollow structure as an anode for superior-performance potassium-ion batteries. *Nanoscale* 2020;12:4309-13. DOI PubMed
67. Hussain N, Liang T, Zhang Q, et al. Ultrathin Bi nanosheets with superior photoluminescence. *Small* 2017;13:1701349. DOI PubMed
68. Zhou, J, Chen, J, Chen, M, et al. Few-layer bismuthene with anisotropic expansion for high-areal-capacity sodium-ion batteries. *Adv Mater* 2019;31:e1807874. DOI
69. Hagiwara R, Tamaki K, Kubota K, Goto T, Nohira T. Thermal properties of mixed alkali bis(trifluoromethylsulfonyl)amides. *J Chem Eng Data* 2008;53:355-8. DOI
70. Xu K. Electrolytes and interphases in Li-ion batteries and beyond. *Chem Rev* 2014;114:11503-618. DOI PubMed
71. Shen C, Cheng T, Liu C, et al. Bismuthene from sonoelectrochemistry as a superior anode for potassium-ion batteries. *J Mater Chem A* 2020;8:453-60. DOI
72. Hosaka T, Kubota K, Kojima H, Komaba S. Highly concentrated electrolyte solutions for 4 V class potassium-ion batteries. *Chem Commun* 2018;54:8387-90. DOI PubMed
73. Zhang R, Bao J, Wang Y, Sun CF. Concentrated electrolytes stabilize bismuth-potassium batteries. *Chem Sci* 2018;9:6193-8. DOI PubMed PMC
74. Jiao T, Wu S, Cheng J, et al. Bismuth nanorod networks confined in a robust carbon matrix as long-cycling and high-rate potassium-ion battery anodes. *J Mater Chem A* 2020;8:8440-6. DOI
75. Xiang X, Liu D, Zhu X, et al. Evaporation-induced formation of hollow bismuth@N-doped carbon nanorods for enhanced electrochemical potassium storage. *Appl Surf Sci* 2020;514:145947. DOI
76. Yang H, Xu R, Yao Y, Ye S, Zhou X, Yu Y. Multicore-shell Bi@N-doped carbon nanospheres for high power density and long cycle life sodium- and potassium-ion anodes. *Adv Funct Mater* 2019;29:1809195. DOI
77. Weppner W, Huggins RA. Determination of the kinetic parameters of mixed-conducting electrodes and application to the system Li_3Sb . *J Electrochem Soc* 1977;124:1569-77. DOI
78. McCulloch WD, Ren X, Yu M, Huang Z, Wu Y. Potassium-ion oxygen battery based on a high capacity antimony anode. *ACS Appl Mater Interfaces* 2015;7:26158-66. DOI PubMed
79. Liu Y, Xu J, Kang Z, Wang J. Thermodynamic descriptions and phase diagrams for Sb-Na and Sb-K binary systems. *Thermochim Acta* 2013;569:119-26. DOI
80. Zheng J, Yang Y, Fan X, et al. Extremely stable antimony-carbon composite anodes for potassium-ion batteries. *Energy Environ Sci* 2019;12:615-23. DOI
81. Han C, Han K, Wang X, et al. Three-dimensional carbon network confined antimony nanoparticle anodes for high-capacity K-ion batteries. *Nanoscale* 2018;10:6820-6. DOI PubMed
82. Yi Z, Lin N, Zhang W, Wang W, Zhu Y, Qian Y. Preparation of Sb nanoparticles in molten salt and their potassium storage performance and mechanism. *Nanoscale* 2018;10:13236-41. DOI PubMed

83. Ko YN, Choi SH, Kim H, Kim HJ. One-pot formation of Sb-carbon microspheres with graphene sheets: potassium-ion storage properties and discharge mechanisms. *ACS Appl Mater Interfaces* 2019;11:27973-81. DOI PubMed
84. Liu Y, Tai Z, Zhang J, et al. Boosting potassium-ion batteries by few-layered composite anodes prepared via solution-triggered one-step shear exfoliation. *Nat Commun* 2018;9:3645. DOI PubMed PMC
85. Yi Z, Qian Y, Tian J, Shen K, Lin N, Qian Y. Self-templating growth of Sb_2Se_3 @C microtube: a convention-alloying-type anode material for enhanced K-ion batteries. *J Mater Chem A* 2019;7:12283-91. DOI
86. Huang H, Wang J, Yang X, et al. Unveiling the advances of nanostructure design for alloy-type potassium-ion battery anodes via in situ TEM. *Angew Chem Int Ed* 2020;59:14504-10. DOI PubMed
87. Liu Q, Fan L, Ma R, et al. Super long-life potassium-ion batteries based on an antimony@carbon composite anode. *Chem Commun* 2018;54:11773-6. DOI PubMed
88. An Y, Tian Y, Ci L, Xiong S, Feng J, Qian Y. Micron-sized nanoporous antimony with tunable porosity for high-performance potassium-ion batteries. *ACS Nano* 2018;12:12932-40. DOI PubMed
89. Wang Z, Dong K, Wang D, et al. A nanosized SnSb alloy confined in N-doped 3D porous carbon coupled with ether-based electrolytes toward high-performance potassium-ion batteries. *J Mater Chem A* 2019;7:14309-18. DOI
90. Ge X, Liu S, Qiao M, et al. Enabling superior electrochemical properties for highly efficient potassium storage by impregnating ultrafine Sb nanocrystals within nanochannel-containing carbon nanofibers. *Angew Chem Int Ed* 2019;58:14578-83. DOI PubMed
91. Cheng Y, Yao Z, Zhang Q, et al. In situ atomic-scale observation of reversible potassium storage in Sb_2S_3 @Carbon nanowire anodes. *Adv Funct Mater* 2020;30:2005417. DOI
92. Liu H, He Y, Cao K, et al. Stimulating the reversibility of Sb_2S_3 Anode for high-performance potassium-ion batteries. *Small* 2021;17:e2008133. DOI
93. Sheng B, Wang L, Huang H, et al. Boosting potassium storage by integration advantageous of defect engineering and spatial confinement: a case study of Sb_2S_3 . *Small* 2020;16:e2005272. DOI
94. Wang T, Shen D, Liu H, Chen H, Liu Q, Lu B. A Sb_2S_3 nanoflower/MXene composite as an anode for potassium-ion batteries. *ACS Appl Mater Interfaces* 2020;12:57907-15. DOI
95. Chen B, Yang L, Bai X, et al. Heterostructure Engineering of Core-Shelled Sb@ Sb_2S_3 encapsulated in 3D N-doped carbon hollow-spheres for superior sodium/potassium storage. *Small* 2021;17:e2006824. DOI
96. He X, Liao J, Wang S, et al. From nanomelting to nanobeads: nanostructured $\text{Sb}_x\text{Bi}_{1-x}$ alloys anchored in three-dimensional carbon frameworks as a high-performance anode for potassium-ion batteries. *J Mater Chem A* 2019;7:27041-7. DOI
97. Wu J, Zhang Q, Liu S, et al. Synergy of binders and electrolytes in enabling micro-sized alloy anodes for high performance potassium-ion batteries. *Nano Energy* 2020;77:105118. DOI
98. Liang S, Cheng Y, Zhu J, Xia Y, Müller-buschbaum P. A chronicle review of nonsilicon (Sn, Sb, Ge)-based lithium/sodium-ion battery alloying anodes. *Small Methods* 2020;4:2000218. DOI
99. Tian H, Xin F, Wang X, He W, Han W. High capacity group-IV elements (Si, Ge, Sn) based anodes for lithium-ion batteries. *J Mater Chem* 2015;1:153-69. DOI
100. Yin L, Song J, Yang J, et al. Construction of Ge/C nanospheres composite as highly efficient anode for lithium-ion batteries. *J Mater Chem* 2021;32:6398-407. DOI
101. Hu Z, Zhang S, Zhang C, Cui G. High performance germanium-based anode materials. *Coord Chem Rev* 2016;326:34-85. DOI
102. Jung H, Allan PK, Hu Y, et al. Elucidation of the local and long-range structural changes that occur in germanium anodes in lithium-ion batteries. *Chem Mater* 2015;27:1031-41. DOI
103. Loaiza LC, Monconduit L, Seznec V. Si and Ge-Based Anode Materials for Li-, Na-, and K-Ion Batteries: A Perspective from Structure to Electrochemical Mechanism. *Small* 2020;16:e1905260. DOI PubMed
104. Wen N, Chen S, Feng J, et al. In situ hydrothermal synthesis of double-carbon enhanced novel cobalt germanium hydroxide composites as promising anode material for sodium ion batteries. *Dalton Trans* 2021;50:4288-99. DOI PubMed
105. Zeng T, He H, Guan H, Yuan R, Liu X, Zhang C. Tunable hollow nanoreactors for in situ synthesis of GeP electrodes towards high-performance sodium ion batteries. *Angew Chem Int Ed* 2021;60:12103-8. DOI PubMed
106. Liu R, Luo F, Zeng L, et al. Dual carbon decorated germanium-carbon composite as a stable anode for sodium/potassium-ion batteries. *J Colloid Interface Sci* 2021;584:372-81. DOI PubMed
107. Yang Q, Wang Z, Xi W, He G. Tailoring nanoporous structures of Ge anodes for stable potassium-ion batteries. *Electrochim Acta* 2019;101:68-72. DOI
108. He C, Zhang JH, Zhang WX, Li TT. GeSe/BP van der Waals heterostructures as promising anode materials for potassium-ion batteries. *J Phys Chem C* 2019;123:5157-63. DOI
109. Zhou Y, Zhao M, Chen ZW, Shi XM, Jiang Q. Potential application of 2D monolayer β -GeSe as an anode material in Na/K ion batteries. *Phys Chem Chem Phys* 2018;20:30290-6. DOI PubMed
110. Hao J, Wang Y, Guo Q, Zhao J, Li Y. Structural strategies for germanium-based anode materials to enhance lithium storage. *Part Part Syst Charact* 2019;36:1900248. DOI
111. Balogun M, Yang H, Luo Y, et al. Achieving high gravimetric energy density for flexible lithium-ion batteries facilitated by core-double-shell electrodes. *Energy Environ Sci* 2018;11:1859-69. DOI
112. Mo R, Rooney D, Sun K, Yang HY. 3D nitrogen-doped graphene foam with encapsulated germanium/nitrogen-doped graphene yolk-shell nanoarchitecture for high-performance flexible Li-ion battery. *Nat Commun* 2017;8:13949. DOI PubMed PMC

113. Seo M, Park M, Lee KT, Kim K, Kim J, Cho J. High performance Ge nanowire anode sheathed with carbon for lithium rechargeable batteries. *Energy Environ Sci* 2011;4:425-8. [DOI](#)
114. Li D, Feng C, Liu HK, Guo Z. Hollow carbon spheres with encapsulated germanium as an anode material for lithium ion batteries. *J Mater Chem A* 2015;3:978-81. [DOI](#)
115. Kim D, Park C. Co-Ge compounds and their electrochemical performance as high-performance Li-ion battery anodes. *Mater Today Energy* 2020;18:100530. [DOI](#)
116. Zhao Z, Ma W, Wang Y, Lv Y, Ma C, Liu X. Boosting the electrochemical performance of nanoporous CuGe anode by regulating the porous structure and solid electrolyte interface layer through Ni-doping. *Appl Surf Sci* 2021;558:149868. [DOI](#)
117. Bensalah N, Matalkeh M, Mustafa NK, Merabet H. Binary Si-Ge Alloys as high-capacity anodes for Li-ion batteries. *Phys Status Solidi A* 2020;217:1900414. [DOI](#)
118. Doherty J, McNulty D, Biswas S, et al. Germanium tin alloy nanowires as anode materials for high performance Li-ion batteries. *Nanotechnology* 2020;31:165402. [DOI](#) [PubMed](#)
119. Rodriguez JR, Qi Z, Wang H, et al. Ge₂Sb₂Se₅ glass as high-capacity promising lithium-ion battery anode. *Nano Energy* 2020;68:104326. [DOI](#)
120. Kim WS, Vo TN, Kim IT. GeTe-TiC-C composite anodes for Li-ion storage. *Materials* 2020;13:4222. [DOI](#) [PubMed](#) [PMC](#)
121. Zhou X, Li T, Cui Y, et al. In situ and operando morphology study of germanium-selenium alloy anode for lithium-ion batteries. *ACS Appl Energy Mater* 2020;3:6115-20. [DOI](#)
122. Lee G, Jun Choi Y, Hwan Kim Y, et al. Amorphization of germanium selenide driven by chemical interaction with carbon and realization of reversible conversion-alloying reaction for superior K-ion storage. *Chem Eng J* 2022;430:132995. [DOI](#)
123. Sultana I, Ramireddy T, Rahman MM, Chen Y, Glushenkov AM. Tin-based composite anodes for potassium-ion batteries. *Chem Commun* 2016;52:9279-82. [DOI](#) [PubMed](#)
124. Wang Q, Zhao X, Ni C, et al. Reaction and capacity-fading mechanisms of tin nanoparticles in potassium-ion batteries. *J Phys Chem C* 2017;121:12652-7. [DOI](#)
125. Ramireddy T, Kali R, Jangid MK, Srihari V, Poswal HK, Mukhopadhyay A. Insights into electrochemical behavior, phase evolution and stability of Sn upon K-alloying/de-alloying via in situ studies. *J Electrochem Soc* 2017;164:A2360-7. [DOI](#)
126. Qin G, Liu Y, Han P, Wang L, Liu F, Ma J. Self-regulating organic polymer coupled with enlarged inorganic SnS₂ interlamellar composite for potassium ion batteries. *Adv Funct Mater* 2020;30:2005080. [DOI](#)
127. Hu R, Fang Y, Liu X, et al. Synthesis of SnS₂ ultrathin nanosheets as anode materials for potassium ion batteries. *Chem Res Chin Univ* 2021;37:311-7. [DOI](#)
128. Verma R, Didwal PN, Nguyen A, Park C. SnSe nanocomposite chemically-bonded with carbon-coating as an anode material for K-ion batteries with outstanding capacity and cyclability. *Chem Eng J* 2021;421:129988. [DOI](#)
129. Lakshmi V, Chen Y, Mikhaylov AA, et al. Nanocrystalline SnS₂ coated onto reduced graphene oxide: demonstrating the feasibility of a non-graphitic anode with sulfide chemistry for potassium-ion batteries. *Chem Commun* 2017;53:8272-5. [DOI](#) [PubMed](#)
130. Cao L, Luo B, Xu B, et al. Stabilizing intermediate phases via efficient entrapment effects of layered VS₄/SnS@C heterostructure for ultralong lifespan potassium-ion batteries. *Adv Funct Mater* 2021;31:2103802. [DOI](#)
131. Sun H, Zhang Y, Xu X, et al. Strongly coupled Te-SnS₂/MXene superstructure with self-autoadjustable function for fast and stable potassium ion storage. *J Energy Chem* 2021;61:416-24. [DOI](#)
132. Cao Y, Chen H, Shen Y, et al. SnS₂ Nanosheets anchored on nitrogen and sulfur Co-doped MXene sheets for high-performance potassium-ion batteries. *ACS Appl Mater Interfaces* 2021;13:17668-76. [DOI](#) [PubMed](#)
133. Zhou S, Lan J, Song K, Zhang Z, Shi J, Chen W. SnS/SnS₂/rGO heterostructure with fast kinetics enables compact sodium ion storage. *FlatChem* 2021;28:100259. [DOI](#)
134. Sun Q, Li D, Dai L, Liang Z, Ci L. Structural engineering of SnS₂ encapsulated in carbon nanoboxes for high-performance sodium/potassium-ion batteries anodes. *Small* 2020;16:e2005023. [DOI](#) [PubMed](#)
135. Wen S, Gu X, Ding X, et al. Constructing ultrastable electrode/electrolyte interface for rapid potassium ion storage capability via salt chemistry and interfacial engineering. *Nano Res* 2022;15:2083-91. [DOI](#)
136. Sheng C, Yu F, Li C, et al. Diagnosing the SEI layer in a potassium ion battery using distribution of relaxation time. *J Phys Chem Lett* 2021;12:2064-71. [DOI](#) [PubMed](#)